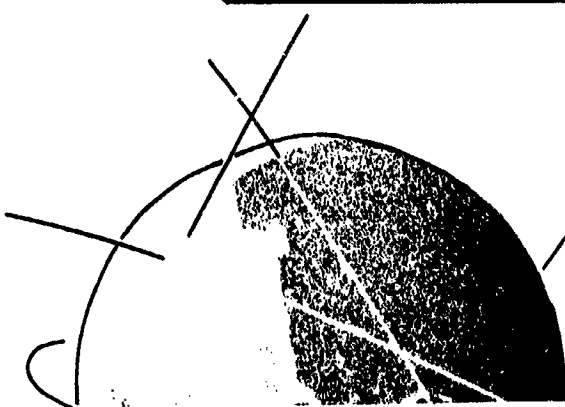
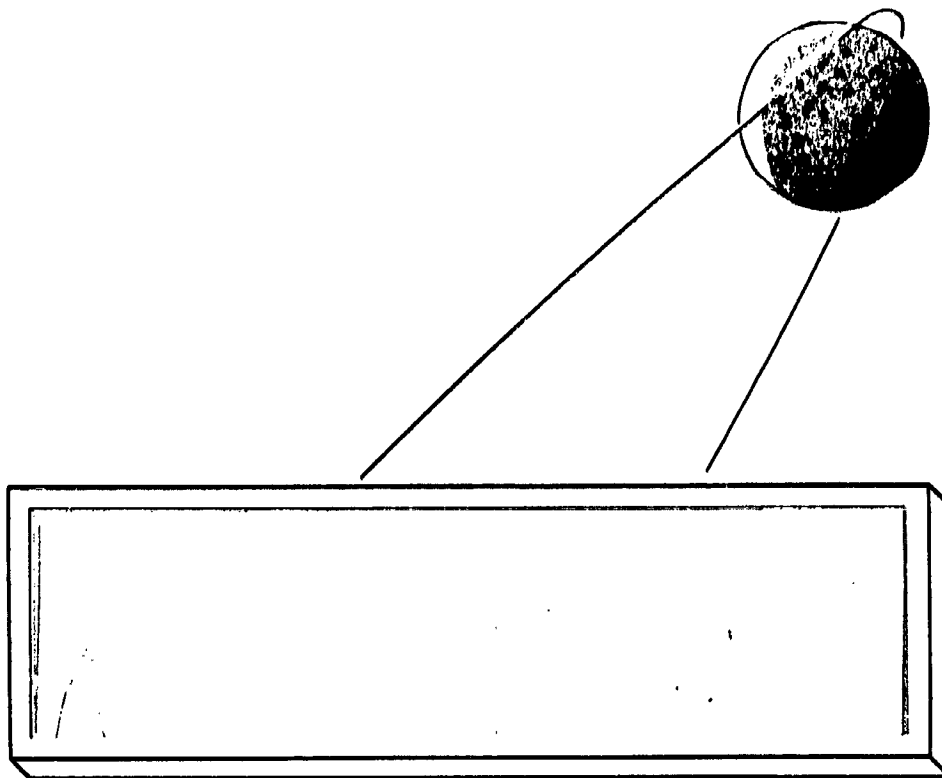


C.R. 115467



OFFICE OF PRIME RESPONSIBILITY

ES3

(NASA-CR-115467) FLOW FIELD MEASUREMENTS  
FOR CYLINDRICAL CONFIGURATIONS IN A  
HYPERSONIC WIND TUNNEL: WINDWARD AND  
LEEWARD FLOW FIELDS J.J. Bertin, et al  
(Texas Univ.) Dec. 1971 76 p CSCL 20D G3/12  
(NASA CR OR TMA OR AD NUMBER) (CITELOC)

N72-20271

Unclass  
20577



FLOW FIELD MEASUREMENTS FOR CYLINDRICAL CONFIGURATIONS  
IN A HYPERSONIC WIND TUNNEL: WINDWARD AND  
LEEWARD FLOW FIELDS\*

by - John J. Bertin, J. Parker Lamb, Kathy R. Center  
and Bruce W. Graumann

\*The authors gratefully acknowledge the financial  
support provided by the National Aeronautics  
and Space Administration through MSC  
Contract NAS 9-10976.

Aerospace Engineering Report 71007

Department of Aerospace Engineering and  
Engineering Mechanics  
The University of Texas at Austin

December 1971

### ACKNOWLEDGEMENTS

The authors would also like to express their gratitude to the personnel of the Hypervelocity Wind Tunnel Group of the Vought Aeronautics Corporation. The efforts of E. Greenwood, J.L. Lindsey, H. Mittel, J. Neuman, T.C. Pope, C.J. Stalmach (supervisor) and L.J. Tieman went beyond contractual minimums. Their interest in and their personal concern for the University's needs are sincerely appreciated.

## TABLE OF CONTENTS

ACKNOWLEDGEMENTS . . . . .	1
INTRODUCTION . . . . .	1
NOMENCLATURE . . . . .	5
EXPERIMENTAL PROGRAM . . . . .	7
Models . . . . .	7
Test Facility . . . . .	10
Test Program . . . . .	10
DISCUSSION OF RESULTS . . . . .	12
Windward Flow Field . . . . .	13
Separation and the Leeward Flow Field . . . . .	23
CONCLUDING REMARKS . . . . .	29
REFERENCES . . . . .	31
TABLES . . . . .	34
FIGURES . . . . .	37

## INTRODUCTION

When designing a vehicle and its thermal protection system for manned reentry, the most desirable configuration minimizes the heating rate and, therefore, does not require active systems (such as film cooling) or degrading systems (such as ablative materials). Complete avoidance of an active or of a degrading thermal protection system is practically impossible. However, the desired low heating-rates can often be achieved for large surface areas by selecting a configuration for which boundary-layer separation leaves large areas in a relatively low-velocity wake flow.

A necessary condition (Ref. 1) for separation of the viscous boundary layer from the wall is an increasing pressure in the streamwise direction, i.e., an adverse pressure gradient along the flow path. The necessary adverse pressure gradient may be due to shock waves associated with a flow recompression subsequent to a rapid expansion at a relatively sharp corner. In general, the separation location depends upon geometric parameters, such as configuration geometry and angle-of-attack, and upon flow parameters, such as free-stream Mach number, Reynolds number, and the wall temperature. At high Mach numbers, the "hypersonic freeze" principle (Ref. 2) indicates that the inviscid flow field is independent of the Mach number. Because of its use as a transition criteria, the Reynolds number is an important parameter in establishing a separation criterion. However, even without transition, the base pressure has been found to be dependent on the Reynolds number, if only weakly (e.g., Refs. 3 and 4).

For the three-dimensional flow of an inclined body of revolution, two distinct separation types have been observed at low speeds by Wang (Ref. 5). The first stage of separation appears to be of a free vortex layer type; the second stage appears to be of a bubble type. Wang notes that other workers have observed qualitatively similar patterns at hypersonic speeds.

An objective of the present study was to examine parameters which influence the extent of separation and the resultant flow in the separated region, yet avoid undue complexities in the flow field. Therefore, it was the intention of the model design to simulate the flow-field for an infinite cylinder. However, the models were of limited length in order to allow that the models would be entirely within the tunnel core and to avoid shock - boundary layer interactions at the tunnel wall, which arise when the model spans the tunnel. Thus, the boundary layer for the windward flow is three dimensional.

A solution of the compressible, three-dimensional boundary layer on the cylinder at angle-of-attack must account for the divergence, or convergence, of the external streamlines which gives rise to a thinning, or thickening, of the boundary layer. A rigorous solution must also account for the skew character of the velocity profile which occurs since the flow in the boundary layer must turn more than the inviscid flow in order to allow the centrifugal force gradient to balance the resultant lateral pressure gradient. Although solutions for the laminar, compressible three-dimensional boundary layer have been obtained (e.g., Ref. 6), the method is very complex. Moreover, it has been found (Ref. 7) that, even for large transverse pressure gradients, the cross-flow can be

neglected in the presence of a highly cooled surface and of moderate Mach numbers at the edge of the laminar boundary layer.

Although quite small in relation to windward heat transfer the leeward heating process is also important to the vehicle designer for the primary reason that unnecessary thermal protection over leeward surfaces could represent a significant weight penalty and therefore should be avoided. Thus, it is desirable to have basic information about the level and extent of convective heating over the leeward side of typical cross sections. Furthermore, since only a limited number of shapes can be examined experimentally one objective of the current study was to provide correlations and generalizations of the test data obtained.

Much of the previous experience with manned reentry vehicles indicates that flow in the near wake is laminar (e.g., Ref. 8). The large favorable pressure gradient which exists upstream of the separation point on most of these configurations tends to insure a laminar boundary layer prior to separation. Furthermore, Lees (Ref. 9) indicated that as the boundary layer separates to become the shear layer, it will remain laminar if the edge Mach number is greater than about 2.5.

The present report investigates the flow-field for "simulated" infinite cylinders over an angle-of-attack range from  $30^\circ$  to  $90^\circ$ . The range of test conditions for the experimental program, which was conducted in the Vought Aeronautics Corporation's Hypervelocity Wind Tunnel (VAC HVWT), includes free-stream Mach numbers from 10 to 15 with unit Reynolds numbers from  $2 \times 10^6$  per foot to  $2 \times 10^7$  per foot.

The analysis of these measurements includes comparison with theoretical correlations and with results from other experimental investigations.



# NOMENCLATURE

- $C_p$  - pressure coefficient
- $F$  - a factor in the heat-transfer equation which accounts for the non-circular shape of the fuselage cross-section, defined in eqn. 6
- $L$  - total model length, measured along the plane of symmetry, or a characteristic separation length (see Fig. 17)
- $M_\infty$  - free stream Mach number
- $P_{t2}$  - stagnation pressure behind a normal shock
- $[q_{Leq}]_{avg}$  - average value of heat-transfer to the surface downstream of boundary-layer separation
- $\dot{q}_{tc\#1}$  - experimental heat-transfer rate for thermocouple no. 1, which is located in the windward plane of symmetry
- $\dot{q}_{t, ref}$  - calculated value of heat-transfer to the stagnation point of a sphere whose diameter is  $W_b$
- $r_c$  - the corner radius for flat-faced configuration with rounded corners
- $Re_\infty/ft$  - free stream unit Reynolds number
- $R_{eff}$  - effective radius of curvature for a fuselage whose cross-section is non-circular
- $s$  - distance from leading edge of the model measured along the fuselage axis
- $s_z$  - distance around the perimeter of the cross-section as measured from the plane of symmetry
- $T_t$  - stagnation temperature

- $u_e$  - streamwise velocity component of the inviscid flow
- $W_b$  - body width
- $W_s$  - characteristic maximum wake width (see Fig. 17)
- $x_{ic}$  - the axial location of the instrumentation on the instrumented core (see Fig. 2)
- $\tilde{y}$ -coordinate - distance from the surface as measured in the plane of symmetry
- $z$ -coordinate - transverse distance from the plane of symmetry
- $\alpha$  - angle of attack
- $\delta_t$  - the shock wave standoff distance in the plane of symmetry
- $\phi$  - polar coordinate for right circular cylinder
- $\phi_s$  - location of boundary layer separation for a right circular cylinder in polar coordinate
- $\nu_e$  - viscosity of fluid at the edge of the boundary layer

## EXPERIMENTAL PROGRAM

The experimental program was conducted to obtain information defining the flow field for four different simulated "infinite" cylinders over an angle-of-attack range from  $30^{\circ}$  to  $90^{\circ}$ . The data generated during the program included measurements for the heat-transfer-rate and surface-pressure distribution and shadowgraphs.

### Models

Dimensioned sketches for the four different cross-sections tested are presented in Fig. 1. The four configurations were: (1) a right-circular cylinder, designated C1, (2) a flat-faced triangular cylinder, designated C2, (3) a "rectangular" flat-faced cylinder representing a typical cross-section of the space shuttle fuselage, designated C3, and (4) a cylinder whose windward surface was a circular segment and whose leeward surface was triangular, designated C4. A brief review of the philosophy used in selecting these cross-sections might be useful at this point. Since the measurements for the right-circular cylinder, C1, could be readily compared with theoretical predictions and experimental results available in the literature, it was chosen as a reference configuration. The C4 cylinder has the same cross-section as the Apollo Command Module. Thus, considerable data are available for comparison if one selects correlation parameters which are independent of whether the flow is two-dimensional or axisymmetric. The C3 cylinder corresponds to a fuselage cross-section of one concept for the McDonnell-Douglas space shuttle orbiter which was available at the time the test program

was initiated. The windward portion of the C2 configuration is identical to that for the C3 configuration; while the leeward surface of the C2 configuration is identical to that for the C4 configuration. Thus, the data for the C2 configuration indicate the independence of the windward and the leeward flow fields.

The body width,  $W_b$ , was chosen as the characteristic length by which parameters relating to model dimensions were divided to obtain dimensionless correlation parameters. The body width was the same for all four configurations, i.e., 1.5 inches. Circumferential distributions are presented as a function of  $s_z$ , which is the wetted distance around the perimeter of the cross-section (Fig. 1). Axial distributions are presented as a function of  $s$ , which is the distance from the leading edge in the plane of symmetry (Fig. 2).

Also presented in Fig. 1 are the circumferential locations of the pressure orifices and of the thermocouples, which were used to determine the local heating rate. The models were constructed such that the thermocouples were on one side of the model, the pressure orifices on the other, providing both types of data during the same shot. Because it was felt that heat-transfer measurement would be more sensitive to the character of the local flow-field, the number of thermocouples on a model was roughly twice the number of pressure orifices. For each pressure orifice location, there was a thermocouple at the same point (in the mirror image). Thus, the pressure data would provide information about the local inviscid flow-field from which the heating-rate measurements were taken. In general, most of the instrumentation was located in a "single" plane, the exceptions being some sensors located in the

corner regions of the models. These were placed  $\pm 0.2$  inch away from the primary instrumentation plane in order to accommodate them physically.

Additional sensors were placed at other stations in order to determine if three-dimensional effects were present. The circumferential locations of these sensors appear at the end of the tables in Fig. 1. The significance of the axial dimension to the instrumentation on the instrumented core ( $x_{ic}$ ) is indicated in Fig. 2.

The local pressures were measured using Sensotech transducers. The semiconductor strain gages of the transducers had a nominal output of one millivolt per psi. The local heating rates were determined from computer fits of the surface-temperature histories. These temperature histories were obtained using thermocouples of 40 gage chromel/constantan wire which were spot welded to the inner surface of the 0.004-inch nickel skin of the models.

All of the instrumentation described above was contained in a two-inch "instrumented segment." To properly simulate "infinite" cylinder at the proper angle-of-attack, the instrumented segment was placed between uninstrumented segments having the same cross-section, as shown in Fig. 2.

By using the uninstrumented segments, the surfaces at both ends of the model were parallel to the free-stream velocity. Because the large diameter models were intended to simulate infinite cylinders, it was necessary to consider perturbations due to end plates or to the model support string. To gain insight for model design, test shots were made using a variety of instrumented models with different end plate and support configurations. Based on the shadowgraphs, it was decided not to

use end plates and to locate the model support sting in the wake at the upstream end of the model. A photograph of a typical model installation is presented in Fig. 3. The total pressure probe and the total temperature probe, which are used to determine flow conditions in the tunnel, also can be seen.

#### Test Facility

The VAC Hypervelocity Wind Tunnel is a hot-shot tunnel with a variable volume arc-chamber to provide relatively constant test conditions. A contoured nozzle is used to accelerate the nitrogen test gas to Mach 8 in an 8.0-inch diameter test section. For free-stream Mach numbers of 10, or greater, the wind-tunnel nozzles are conical with a total included angle of  $7.50^\circ$  and the test-section is 12.5 inch in diameter. The high energy capacity of the tunnel provides either a high unit Reynolds number capability, e.g., nominally a unit Reynolds number of  $70 \times 10^6$  per foot at Mach 8, or relatively long run times, e.g., 0.50 second at Mach 17. The facility is complemented by an on-site IBM digital computer which is employed for data acquisition and reduction.

#### Test Program

A run schedule is presented in Table 1 for the nominal test conditions discussed in the present report. The numbers which appear in this table are those assigned by the facility to identify the particular shot for that nominal condition. Table 2 contains the exact test conditions for each run in the schedule.

As noted previously, the nickel skin of the model was only 0.004-inch thick. Because of particle impingement and high surface pressures, model degradation occurred during the course of the test program. In post-test observations of the model, the supervisor of the VAC HVWT briefly discussed the model surface conditions in the data transmittal package, noting "minor skin wrinkling occurred on the C4 model at  $\alpha = 30^\circ$ ." As can be seen in the flow-field photographs presented in Fig. 4 (which are for the C4 model at  $\alpha = 30^\circ$ ), numerous shock waves were generated due to the skin wrinkling. The high Reynolds number test, from which photograph of Fig. 4b was taken, was the later of the two. The greatly disturbed flow-field is attributed to model degradation, the effect of which is amplified by the relatively thin boundary layer at the highest Reynolds number. This skin wrinkling and associated flow-field perturbations significantly influence the measured heat-transfer, which is very sensitive to surface roughness of the scale experienced. These perturbations significantly limit the ability to interpret the effect of flow parameters, as will be discussed more subsequently.

## DISCUSSION OF RESULTS

Since the instrumentation was distributed circumferentially around the entire model, data are available which describe the flow field for the windward surface, for which the boundary layer is attached, as well as for the leeward surface, where evaluation of the flow parameters is complicated by boundary-layer separation. The discussion which follows is therefore divided into the natural categories: "Windward Flow Field" and "Separation and the Leeward Flow Field." As noted when describing the models, the windward surface of the C2 cylinder is identical to that of the C3 configuration; while the leeward portion of the C2 configuration is geometrically identical to that for the C4 configuration. Since the inviscid flow in the separation zone (which divides the "two" flow fields) is supersonic, it was expected that the windward flow field would be essentially the same for the C2 and for the C3 configurations and that the leeward flow field for the C2 and for the C4 configurations would be essentially the same. As discussed subsequently, this expectation was generally verified experimentally, within the accuracy of the data.

The flow field for the windward surface of infinite cylinders at an angle-of-attack of  $90^\circ$  can be solved analytically, because of the planar symmetry of the two-dimensional flow. Therefore, of all the data which were obtained in the present program those which describe the windward flow-field are most amenable to direct correlation with theory. The comparisons between the theoretical calculations and the windward data for these simulated "infinite" cylinders at an angle-of-attack of  $90^\circ$



provide an insight into the character of the flow. Furthermore, such comparisons provide a measure of the validity of the experimental results.

Although the models used in the test program were to simulate "infinite" cylinders, the length-to-width ratios were below the values of 10 suggested in Ref. 3. The model lengths were limited to insure the models would be wholly within the tunnel core. Further, to accommodate the desired instrumentation, the model cross-section was made as large as possible. Thus, the length-to-width ratio varied from only 2.33 for the model used for an angle-of-attack of  $90^\circ$  to 7.33 for the model used for an angle-of-attack of  $30^\circ$ . Because of the relatively short models, the flow field measurements reflected the three-dimensional character of the flow even at an angle-of-attack of  $90^\circ$ .

#### Windward Flow Field

Theoretical solutions of the windward, inviscid flow field for infinite cylinders were obtained using a numerical routine generously supplied by Dr. Gino Moretti. The desired theoretical flow field was calculated using a time-dependent technique (e.g., Ref. 10 to 12) to obtain the limiting solution, which is effectively the steady state solution. The computed shock waves are compared in Fig. 5 with the experimental shock waves for the cylinders at an angle-of-attack of  $90^\circ$ , as recorded photographically. As would be expected, the shock-wave for the C2 configuration is essentially the same as that generated by the C3 configuration. Further, at the high Mach numbers and high Reynolds numbers of the present experimental program, the measured shock

wave is essentially independent of the free-stream conditions for a given configuration, e.g., the results for the C4 cylinder presented in Fig. 5b.

The experimental shock wave is consistently closer to the body than is the theoretical shock wave. The possibility that these differences were due to viscous effects was considered. In a series of calculations by Li (Ref. 13), a noticeably smaller shock layer was obtained because of the wall temperature diffusing upstream, bringing up the density level in the shock layer (but these calculations were for relatively low Reynolds numbers). The displacement thickness of the viscous boundary layer calculated for the present test conditions using the University's numerical code for nonsimilar laminar flow (Ref. 14), was very small in magnitude (sometimes assuming positive values, other times negative values). These values which indicate a negligible displacement thickness for the boundary layer are consistent with the calculations of Li for higher Reynolds numbers. The fact that the observed shock standoff distance is approximately 20% less than the theoretical value for an infinite cylinder is therefore attributed to three-dimensional effects, which are due to the small length-to-width ratios, noted previously.

The pitch plane standoff distance ( $\delta_t$ ) is presented in Fig. 6 as a function of the effective radius of curvature for the windward forebody. The shock standoff distance measured in the plane of symmetry is presented for all three angles-of-attack and for all but the highest Reynolds number. The highest Reynolds number results are not included because the other measurements indicated no significant

Reynolds number effect and because of the difficulty in interpreting the photographs (refer to Fig. 4).

For the fuselage cross-sections which are flat-faced cylinders with rounded corners, the effective radius of curvature is assumed to be (Ref. 15):

$$\frac{R_{\text{eff}}}{0.5W_b} = \frac{2.315}{0.745 + 3.14 \frac{r_c}{W_b}} \quad (1)$$

It might be noted that this equation also applies for the limiting case of a right-circular cylinder, in which case  $r_c = 0.5W_b$  and, therefore,  $R_{\text{eff}} = 0.5W_b$ . For a cross-section which is a circular segment subtending an included angle significantly less than  $90^\circ$ , the effective radius of curvature accounts for the increased velocity gradient. The graphical relation of Ref. 16 (based on experimental results for axisymmetric configurations) has been used to calculate  $R_{\text{eff}}$  for the two-dimensional C4-configuration.

The procedures used to obtain values for the effective radius of curvature are most applicable to the flow for an angle-of-attack of  $90^\circ$ . Nevertheless, a consistent correlation between the standoff distance and the effective radius of curvature is obtained for all three angles-of-attack. As discussed previously, the measurements for  $\alpha=90^\circ$  (presented in Fig. 6c) are less than the theoretical values, which is attributed to the three-dimensional character of the actual flow.

The complete circumferential pressure distributions (in polar coordinates) for the right circular cylinder (configuration C1) are

presented in Fig. 7 for all three angles-of-attack. The present data are compared with the measurements of Penland (Ref. 17) and with modified Newtonian flow theory. For a right circular cylinder at angle-of-attack,

$$C_p = C_{p_{0\alpha}} \cos^2 \phi \quad (2)$$

where  $C_{p_{0\alpha}}$ , the pressure coefficient for the stagnation line at the given angle-of-attack, is related to the pressure coefficient for a stagnation point downstream of a normal shock by:

$$C_{p_{0\alpha}} = C_{p_0} \sin^2 \alpha \quad (3)$$

Although the present data exhibit variations exceeding those usually associated with pressure measurements, the data correlate reasonably well with the other distributions. These differences between the pressure measurements at a given angle-of-attack are attributed to experimental uncertainties rather than to the flow parameters. This assumed independence of Mach number and of Reynolds number is consistent with the findings of others, e.g., Ref. 18.

The experimental pressure distributions from the region where the boundary layer is attached are presented in Fig 8 for all four configurations at an angle-of-attack of  $90^\circ$ . Also included in the figure are the theoretical pressure distributions calculated using both the time-dependent numerical code provided by Moretti and the modified Newtonian flow theory. The measurements usually fall between the two theoretical

distributions. Since the cross-section of the C4 cylinder is the same as that for the Apollo Command Module, the pressure distributions were expected to be the same although one flow is two-dimensional while the other is axisymmetric. As expected, the pressure data are essentially the same for both configurations except in the corner region, where the present pressures are significantly lower than the Apollo data (Ref. 19). The variations in the pressures measured on the C4 cylinder are attributed to experimental scatter. These variations are not rare for a hot-shot type facility (a similar correlation exists for pressure measurements on a sharp cone in this tunnel, Ref. 20), although they probably represent the upper bound of the expected scatter. The windward pressure data for all four configurations appear to be independent of the Reynolds number.

Because of the cylindrical nature of the models, at a given angle-of-attack, the angle between the surface tangent of the plane of symmetry and the free-stream velocity vector is the same for all four configurations. Thus, using a "theoretical" model which assumes that the flow is turned by a straight-line surface element to an angle  $\alpha$  from the free-stream direction, the calculated surface pressure would be independent of configuration cross-section. The pressure data from the plane of symmetry are compared in Fig. 9 with the pressures calculated for three simple flow-models, specifically, modified Newtonian flow, tangent cone, and tangent wedge. The values calculated using the equation for modified Newtonian flow (Eq. 3) provide the best correlation with the data. Also included for comparison are pressure data obtained in a companion study (Ref. 21) of blunt cylindrical fuselages with

similar cross-sections.

As noted previously, data were obtained over a wide range of Reynolds number. The forebody pressure measurements were seen to be independent of Reynolds number, as would be expected. As can be seen in Fig. 10, the heat-transfer-rate distribution is dependent on the Reynolds number. To minimize the run-to-run variations when comparing nondimensionalized heat-transfer-rate distributions for a given configuration at two different flow conditions, the local measurements have been divided by the heat-transfer-rate measured in the plane of symmetry, i.e., at thermocouple 1, rather than by a theoretical reference heating rate (as was usually done for the other figures). Although division of a measurement by a theoretical reference heating rate should eliminate the dependence on the free-stream conditions, the resulting dimensionless value would reflect experimental inaccuracies (differences between a particular run and theory). Referencing the measurement to a correlatable experimental value obtained during the same run reduces the effect of experimental variations, although it is not completely eliminated.

The experimental heat-transfer-rate distributions, thus nondimensionalized, are presented in Fig. 10 for both the C1 and the C4 configurations at an angle-of-attack of  $90^\circ$ . Included for comparison is the theoretical heat-transfer distribution for a laminar boundary layer as calculated using the method of Lees (Ref. 22). The experimental pressure distributions of Fig. 8 have been used to compute the required properties of the inviscid flow at the edge of the boundary layer. Consider first the measurements for the right circular cylinder, i.e., the

C4 configuration. The lower Reynolds number distribution clearly indicates that the boundary layer is laminar. At the higher Reynolds number, the heat-transfer data indicate boundary layer transition with subsequent relaminarization due to a large favorable pressure gradient. By the parameter  $K$  (Ref. 23), where

$$K = \frac{v_a}{u_a^2} \frac{du_a}{ds_z},$$

the velocity gradient exceeds the value for which relaminarization of a boundary layer has been observed on a cylindrical body in an accelerated flow (Ref. 23). Therefore, agreement between the dimensionless heat-transfer rates just upstream of boundary layer separation (i.e.,  $s_z \sim 0.7 W_D$ ) is attributed to the fact that transition reversal back to a laminar boundary layer occurs at the higher Reynolds number.

The heat-transfer measurements for the C4 cylinder at an angle-of-attack of  $90^\circ$  exhibit similar characteristics, as can be seen in Fig. 10b. The lower Reynolds number data for the present two-dimensional configuration compare favorably with the results for the axisymmetric Apollo configuration (Ref. 19). Because the boundary layer was laminar for the Apollo tests, it is assumed that it is also laminar for the present two lower Reynolds number tests. Although the heat-transfer measurements at the highest Reynolds number qualitatively follow the theoretical laminar distribution, the boundary layer is believed to be transitional, if not fully turbulent. The dimensionless heat-transfer rate for the last thermocouple is roughly the same for all three Reynolds numbers. Again, the large favorable pressure

gradient has promoted relaminarization of the boundary layer, as can be seen by the diminishing variation between the measurements for the different Reynolds numbers. However, since the difference has not completely vanished, it is impossible to conclude from these data that the boundary layer just prior to separation is indeed laminar for all three conditions.

Since a primary objective of the study was to define the extent of boundary-layer separation and the character of the separated flow, most of the instrumentation was in a "single" plane. However, additional thermocouples were placed at other stations on the instrumented segment in order to determine if three-dimensional effects were present. The axial heat-transfer-rate "distribution" measured in the windward plane of symmetry of the C4 cylinder at an angle-of-attack of  $30^\circ$  is presented in Fig. 11. The data at an angle-of-attack of  $30^\circ$  (for which the model is the longest) clearly indicate the three-dimensional character of the boundary layer. Included for comparison are theoretical distributions for laminar flow calculated using the tangent-cone and the tangent-wedge flow-field assumptions, as well as the swept-cylinder relation. (These techniques are discussed in more detail in Ref. 21.) The experimental distribution is in good agreement with the theoretical values calculated for the tangent-cone model. Although the data compare almost as well with the values calculated for the tangent-wedge model, this flow model is rejected on the basis of the lack of correlation of the pressure measurements, refer to Fig. 9. At points well downstream of the stagnation point, the heating on a space-shuttle orbiter whose fuselage had a C4 cross-section showed similar agreement with tangent-cone theory while similarly falling below the swept-cylinder



value (ref. 21).

The pitch-plane heat-transfer-rate distributions at an angle-of-attack of  $60^\circ$  are presented in Fig. 12 for the C4 cylinder (rounded forebody) and for the C2 and the C3 cylinders (both having a flat-faced forebody). Comparison of the heat-transfer data for these cross-sections indicates:

- (1) that boundary-layer transition occurs earlier for the rounded cross-section than for the flat-bottomed configurations, and
- (2) that the laminar heat-transfer measurements are roughly 30% below the theoretical swept-cylinder values.

Similar results were observed for fuselages of similar cross-section on a straight-winged orbiter at similar angles-of-attack (Ref. 21).

The heat-transfer measurements from the plane of symmetry of the C4 and the C1 cylinders are presented as a function of the angle-of-attack in Fig. 13. As noted when discussing the shock stand-off distances, because of the relatively short length of the models tested at an angle-of-attack of  $90^\circ$ , three-dimensional effects do exist. However, the variation between the stagnation-line measurements for the two Reynolds numbers are believed to be indicative of the experimental uncertainty.

Included for comparison are a linear correlation:

$$\dot{q} = 0.707 F(\dot{q}_{t,ref}) \frac{\alpha}{90^\circ} \quad (4)$$

and the swept-cylinder relation:

$$\dot{q} = 0.707 F(\dot{q}_{t,ref}) (\sin \alpha)^{1.2} \quad (5)$$

The factor 0.707 represents the ratio of heat transfer to a two-dimensional configuration to that to an axisymmetric configuration having the same cross-section. Although other values for this factor appear in the literature, this value is obtained from boundary layer theory with a few, realistic assumptions. The factor  $(\sin \alpha)^{1.2}$  represents the effect of angle-of-attack, or sweep, as taken from Ref. 24. The product  $F\dot{q}_{t,ref}$  represents the theoretical heating rate to an axisymmetric configuration having the same cross-section as the "infinite" cylinder. The relations of Fay and Riddell (Ref. 25) are used to calculate  $\dot{q}_{t,ref}$ , which is the theoretical heating rate to the stagnation point of a sphere whose diameter is  $W_b$ . The factor  $F$  accounts for the noncircular shape of the cross-section and is, therefore,

$$F = \sqrt{\frac{0.5W_b}{R_{eff}}} \quad (6)$$

As would be expected the value of  $F$  is unity for the right circular cylinder, while it is 0.685 for the C4 cylinder. Theoretical values of the heat-transfer to the stagnation line of the C4 configuration at an angle-of-attack of  $90^\circ$  have been calculated for three different values of the effective radius of curvature. The theoretical values, which are presented in Fig. 13b, assumed values for  $R_{eff}$  of:

- (1) 0.0625 ft, which is one-half the body width (refer to Fig. 1),
- (2) 0.1500 ft, which is the physical radius of curvature for the windward surface (refer to Fig. 1), and
- (3) 0.1333 ft, which is the effective radius of curvature based on an experimental study employing axisymmetric models (Ref. 16).

Comparison of the stagnation-line calculations with the measurements supports the use of an  $R_{\text{eff}}$  of 0.1333 feet, which corresponds to an  $F$  of 0.685. Thus, it appears that the axisymmetric factors may be used for two-dimensional configurations as well.

At the present thermocouple locations, the laminar heat-transfer rates measured at the lower Reynolds number are best approximated by the linear relation. The correlation with the linear relation would depend on the thermocouple location. The turbulent character of the boundary layer for the high Reynolds-number data causes the heat-transfer measurements at angle-of-attack to exceed both "theoretical" correlations.

#### Separation and the Leeward Flow Field

One of the major problems in any experimental study of separated flow fields is the low absolute values of the parameters, e.g., pressure or heat transfer rate, which must be measured. An error which may be extremely small in absolute value can represent a highly magnified percentage error. Thus, one usually expects a somewhat greater degree of scatter in leeward data than in the corresponding windward information. The measurement uncertainty is further amplified when one is employing a blowdown tunnel which generally introduces an additional increment of uncertainty due to the lack of absolute repeatability. Because of these inherent measurement difficulties it was found desirable to compute average heat transfer rates over the leeward surface and employ these average values as characteristic parameters for comparison and correlation. This approach is not unreasonable in view of the near constancy of surface pressure and heat transfer levels within fully separated regions.

In computing average leeward heat transfer rates it is of course necessary to determine where separation occurs. Of the four configurations considered in the current study, defining the separation location for the right-circular cylinder presented the most difficulty. The experimental pressure distributions may be used to locate approximately the point at which boundary-layer separation occurs. The pressure data for the right circular cylinder, configuration C1 in Fig. 7, indicate that the separation is dependent on the angle-of-attack. The separation location appears to move slightly downstream as the angle-of-attack increases. However, this conclusion (which is supported by the data of Fig. 7) is made with the knowledge that the angle-of-attack dependence has been noted by others, as discussed below. Because of the experimental uncertainty such a conclusion could not be drawn from the present data alone. Based on the current data alone, the separation point is approximately  $103^\circ$  from the stagnation line for all angles-of-attack. This value results from the current estimation technique which ignores the region of sub-base pressure, indicated in references 3 and 17 as occurring just prior to separation. The differences between the separation angle assumed for this integration of the present data and those reported in the literature (e.g., Refs. 17 and 18) do not substantially affect the average heat-transfer rates.

Penland (Ref. 17) noted, "The point of separation appears to vary from about  $120^\circ$  from the stagnation point for an angle-of-attack of  $90^\circ$  to about  $100^\circ$  from the stagnation point for an angle-of-attack of  $14.9^\circ$ ." Furthermore, the measurements of Beckwith and Gallagher (Ref. 18) indicate that flow separation occurs near a  $\phi$  of  $100^\circ$ . Thus, although the

functional dependence on angle-of-attack of the current separation locations is consistent with the findings of others, the specific separation locations differ somewhat.

Oil flow patterns subsequently obtained in the Supersonic Wind Tunnel of the University of Texas at Austin indicate the surface streamlines near the separation line were almost perpendicular to the axis of the C1 cylinder. Thus, the placement of a sting in the wake might increase the leeward pressure slightly (for this configuration) and, therefore, move the separation location upstream (as appeared to be the case for the VAC models). These tests further indicate that cross flow and, thus, the effect of sting placement are dependent on the cross-section.

Pressure distributions for the afterbody of the C3 configurations are presented in Fig. 14. Also indicated in the figure are the instrumentation locations and the position of the tangency points. For an angle-of-attack of  $60^\circ$ , the pressure distribution indicates a separation bubble followed by a recompression region at each of the expansion corners on the lateral surface. Although the nondimensionalized pressure values are somewhat higher, the experimental distribution at an angle-of-attack of  $90^\circ$  does not indicate the existence of separation bubbles at the expansion corners. At both angles-of-attack, the data indicate that the boundary layer does not clearly separate until reaching the circular cap, i.e., the extreme leeward surface.

The corresponding heat-transfer distributions are presented in Fig. 15. The dimensionless heating rates are also somewhat higher for the  $90^\circ$  angle-of-attack test. The oil flow tests in the University's

Supersonic Wind Tunnel indicated a complex three-dimensional flow at the lower angle-of-attack. Despite the difference in the pressure distributions, the heat-transfer distributions for the two angles-of-attack are qualitatively very similar. At both angles-of-attack the recompression downstream of the first expansion produces a significant increase in the local heating. These data also support the contention that the boundary layer does not separate until reaching the circular cap.

It has been shown that the measurements from the forebody of the C4 configuration at an angle-of-attack of  $90^\circ$  compare favorably with data for the Apollo Command Module at zero angle-of-attack. This agreement between the nondimensionalized data for a two-dimensional flow with those for an axisymmetric flow holds for the leeward surface as well. The surface-pressure and the heat-transfer-rate distributions for the leeward surface of the C4 configuration are compared with the Apollo data in Fig. 16. The differences are believed to be within the accuracy of the leeward measurements (which has been discussed already).

Having established the location of separation, one can evaluate the characteristic lengths  $L$  and  $W_s$ , which are shown in Fig. 17 for each cross section. Use of these parameters is suggested by theoretical concepts embodied in Reference 26. Although devoted to base heat transfer for turbulent flow, the qualitative features of this flow model are applicable to current geometries and flow conditions. The model of Ref. 26 suggests that the primary length parameters for leeward heat transfer are (1) the distance from the wake stagnation point (the impingement of the free shear layers) to the rear stagnation point of the body

and (2) a characteristic maximum wake width. The former distance cannot be obtained, in general, without extensive flow visualization or wake probing and therefore is not readily available. For the present flow geometries and conditions one would expect that, as a consequence of the "hypersonic freeze" principle (see Ref. 3), the wake stagnation point is approximately the same distance (when normalized with the appropriate width) from the separation point for each cylindrical shape. Therefore, the dimensionless length  $L/W_g$  is inversely proportional to the desired distance from body surface to the wake stagnation point.

Correlation of leeward heat-transfer rates for the various cylinders is shown in Fig. 18 where, for a given value of  $\alpha$ , the average heat transfer rate, normalized with respect to the reference value, is plotted versus the ratio of characteristic lengths. The average heating for the leeward region is nondimensionalized using the relation:

$$\frac{[\dot{q}_{\text{Lee}}]_{\text{avg}}}{\dot{q}_{t,\text{ref}}} = \frac{\int_{s_{z,1}}^{s_{z,2}} \dot{q} \, ds}{\dot{q}_{t,\text{ref}} \int_{s_{z,1}}^{s_{z,2}} ds} \quad (7)$$

where  $s_{z,1}$  is the location of boundary-layer separation and  $s_{z,2}$  is the coordinate of the leeward stagnation point. Although no Reynolds number effect is evident because of the measurement problems alluded to earlier, the systematic variation of heat transfer which emerges from this type of plot provides strong evidence of the validity of the two characteristic lengths. Further confirmation is obtained from the data of Holloway, Sterrett and Creekmore (Ref. 27) which are also presented in Fig. 18. These measurements represent heat transfer immediately downstream of a backstep in hypersonic laminar flow and correspond to a blunt-base geometry, i.e.,  $L \equiv 0$ , at a  $90^\circ$  angle-of-attack.

Along with the windward boundary layer relaminarization noted in Fig. 10, the Holloway data also support the conclusion that the near wake was fully laminar for all tests in the current series. Further support for this assertion can be obtained from the shear-layer transition criterion of Lees (Ref. 9) which proposes that, for a hypersonic blunt body, the near wake is laminar if the Mach number adjacent to the free shear layers is above 2.5. The present leeward pressure data, e.g., Figs. 14 and 16, are indeed indicative of such Mach numbers and, hence, laminar shear layers.

The heat-transfer parameter of Fig. 18 is displayed as a function of angle-of-attack in Fig. 19. The similarity of C2 and C4 leeside heating is obvious as is the nearly linear variation with  $\alpha$ . This latter feature suggests that, for a given configuration, the ratio of heat-transfer rate at any value of  $\alpha$  to the value at  $\alpha=90^\circ$  should also be linear. This is indeed true, as shown in Fig. 20. Furthermore, within the scatter of the present data, the slope of the linear variation is virtually the same for all configurations.



### CONCLUDING REMARKS

The experimental program included both windward and leeward measurements for a variety of simulated "infinite" cylinders exposed to hypersonic streams over an angle-of-attack from  $30^{\circ}$  to  $90^{\circ}$ . For the range of conditions included in this study, the following conclusions are made.

- (1) Swept-cylinder theory provides a reasonable correlation of the measured laminar heat-transfer rates from the plane of symmetry. However, if one uses the tangent-cone or the tangent-wedge techniques to account for the three-dimensional nature of the flow along this windward-most element, improved correlation with the measurements is obtained.
- (2) The boundary layer transition criteria in the plane of symmetry are a function of the transverse curvature. For a given flow condition, transition occurred earlier for the cylinder whose windward surface was a circular segment than for the cylinder whose windward surface was flat.
- (3) Relaminarization of the circumferential boundary layer for a right-circular cylinder was observed at the highest Reynolds number tested. Although the boundary layer on the forebody was naturally turbulent, the large pressure gradients produced transition reversal on the windward surface.
- (4) The effect of leeside geometry on the average heat-transfer rate can be correlated with a single geometric parameter which is dependent on the location of separation.

(5) The relationship of leeward heating to angle-of-attack is found to be virtually linear for each cross-section. This variation is essentially the same as that for laminar heating in the plane of symmetry.

(6) No systematic effect of free-stream Reynolds number on the foregoing relationships was observed. The heat-transfer data indicated that the near wake was laminar.

## REFERENCES

1. P. K. Chang: Separation of Flow, Chapter 1, Pergamon Press, Oxford, Great Britain, 1970.
2. W. D. Hayes and R. F. Probstein: Hypersonic Flow Theory, I - Inviscid Flow, Chapter 1, Academic Press, New York, 1966.
3. C. F. Dewey, Jr.: "Near Wake of a Blunt Body at Hypersonic Speeds," AIAA Journal, Vol. 3, No. 6, June 1965, pp. 1001-1010.
4. L. L. Kavanau: "Base Pressure Studies in Rarefied Supersonic Flows," Journal of the Aerospace Sciences, Vol. 23, No. 3, March 1956, pp. 193-207, 230.
5. K. C. Wang: "Separation Patterns of Boundary Layer over an Inclined Body of Revolution," AIAA Paper 71-130, presented at the 9th Aerospace Sciences Meeting, New York, January 1971.
6. J. Der, Jr.: "A Study of General Three-Dimensional Boundary Layer Problems by an Exact Numerical Method," AIAA Paper 69-138, presented at the 7th Aerospace Sciences Meeting, New York, January 1969.
7. T. K. Fannelop: "A Method of Solving the Three Dimensional Laminar Boundary Layer Equations with Application to a Lifting Reentry Body," AIAA Journal, Vol. 6, No. 6, June 1968, pp. 1075-1084.
8. J. J. Bertin: "Wind-Tunnel Heating Rates for the Apollo Spacecraft," TMX-1033, January 1965, NASA.
9. L. Lees: "Hypersonic Wakes and Trails," AIAA Journal, Vol. 2, No. 3, March 1964, pp. 417-428.
10. G. Moretti and M. Abbett: "A Time-Dependent Computational Method for Blunt Body Flow," AIAA Journal, Vol. 4, No. 12, December 1966, pp. 2136.
11. G. Moretti: "Inviscid Blunt Body Shock Layers," PIBAL Report 68-15, June 1968, Polytechnic Institute of Brooklyn.
12. G. Moretti: "The Choice of Time-Dependent Technique in Gas Dynamics," PIBAL Report 69-26, July 1969, Polytechnic Institute of Brooklyn.
13. C. P. Li: "Numerical Solutions of the Navier-Stokes Equations for the Shock Layer," TR-675-44-459, August 1971, Lockheed Electronics Company (Houston).

14. J. J. Bertin and O. E. Byrd, Jr.: "The Analysis of a Nonsimilar Boundary Layer, A Computer Code (NONSIMBL)," Aerospace Engineering Report 70002, August 1970, The University of Texas at Austin.
15. M. H. Bertram, W. V. Feller, and J. C. Dunavant: "Flow Fields, Pressure Distributions, and Heat Transfer for Delta Wings at Hypersonic Speeds," TMX-316, September 1960, NASA.
16. J. C. Boison and H. A. Curtiss: "An Experimental Investigation of Blunt Body Stagnation Point Velocity Gradient," ARS Journal, Vol. 29, No. 2, February 1959, pp. 130-135.
17. J. A. Penland: "Aerodynamic Characteristics of a Circular Cylinder at Mach Number 6.86 and Angles of Attack Up to  $90^\circ$ ," RM L54A14, March 1954, NACA.
18. I. E. Beckwith and J. J. Gallagher: "Local Heat Transfer and Recovery Temperatures on a Yawed Cylinder at a Mach Number of 4.15 and High Reynolds Numbers," TR R-104, 1961, NASA.
19. J. J. Bertin: "The Effect of Protuberances, Cavities, and Angle-of-Attack on the Wind-Tunnel Pressure and Heat-Transfer Distribution for the Apollo Command Module," TMX-1243, October 1966, NASA.
20. J. J. Bertin, M. H. McCloskey, C. J. Stalmach, Jr., and R. L. Wright: "Effect of Mass-Addition Distribution and Injectant on Heat Transfer and Transition Criteria," AIAA Paper 72-183 presented at the AIAA 10th Aerospace Sciences Meeting, San Diego, January 1972.
21. J. J. Bertin, F. E. Williams, R. C. Baker, C. L. Smith, and T. C. Pope: "Aerothermodynamic Measurements for Space-Shuttle Configurations in Hypersonic Wind Tunnels," Aerospace Engineering Report 71006, September 1971, The University of Texas at Austin.
22. L. Lees: "Laminar Heat Transfer over Blunt-Nosed Bodies at Hypersonic Flight Speeds," Jet Propulsion, Vol. 26, No. 4, April 1956, pp. 259-269, 274.
23. H. L. Wesoky and C. May: "Boundary Layer Measurements in an Accelerated Flow With and Without Heat Transfer," TND-7030, January 1971, NASA.
24. C. H. Young, D. H. Reda, and A. M. Roberge: "Hypersonic Flow Field and Heat Transfer Studies on a Lifting Entry Vehicle at Angles-of-Attack from  $0^\circ$  to  $60^\circ$ ," GDC-ERR-1418, September 1970, General Dynamics, Convair Division.

25. J. A. Fay and F. R. Riddell: "Theory of Stagnation Point Heat Transfer in Dissociated Air," Journal of the Aeronautical Sciences, Vol. 25, No. 2, February 1958, pp. 73-85, 121.
26. J. P. Lamb, C. G. Hood, and M. G. Johnson: "A Convective Transport Model for Turbulent Supersonic Planar Base Flows," ASME Paper 70-HT/SpT-35, Space Technology and Heat Transfer Conference, Los Angeles, June 1970.
27. P. F. Holloway, J. R. Sterrett, and H. S. Creekmore: "An Investigation of Heat Transfer within Regions of Separated Flow at a Mach Number of 6.0," TN D-3074, NASA, 1965.

Table 1. -- Run Schedule of Nominal Test Condition (VAC HVWT)

Nominal test condition*					
Configuration	$\alpha$	Condition 1	Condition 2	Condition 3	Condition 4
C1	30	—	—	—	1008
	60	4, 2	1004	—	1002
	90	—	1005	—	1006
C2	30	—	1042	1043	1041
	60	16, 15	1045	1044	1046
	90	—	1047	—	1049
C3	30	—	1021	1022	1023
	60	18, 17	1027	1026	1025
	90	—	1028	—	1032
C4	30	8, 9	1012	1011	1010
	60	5	1015	1016	1017
	90	13, 12	1020	—	1019

\*The nominal test conditions are

	$M_\infty$	$Re_\infty/ft$
Condition 1	15	$4.0 \times 10^6$
Condition 2	10	$2.0 \times 10^6$
Condition 3	10	$5.0 \times 10^6$
Condition 4	10	$20.0 \times 10^6$

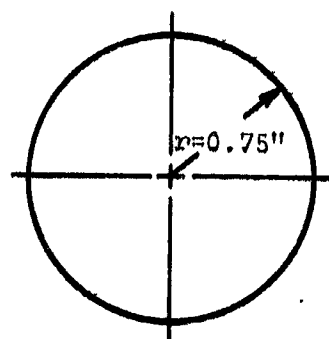
Table 2. -- Run Schedule

Conf	$\alpha$	Run No.	$M_\infty$	$Re_\infty/ft$ $\times 10^{-6}$	$P_{t2}$ (psia)	$T_t$ (°R)
C1	30°	1008	10.10	19.73	55.33	2188
C1	60°	1004	10.00	2.17	15.63	3725
C1	60°	1002	10.10	19.31	46.12	1985
C1	60°	4	14.98	3.96	12.01	3530
C1	90°	1005	10.00	2.17	15.42	3715
C1	90°	1006	10.21	19.16	46.41	2057
C2	30°	1042	10.16	2.15	14.20	3602
C2	30°	1043	10.48	4.33	17.11	2800
C2	30°	1041	9.96	17.31	54.37	2311
C2	60°	1045	10.20	2.47	14.57	3410
C2	60°	1044	10.52	4.81	17.24	2658
C2	60°	1046	9.94	19.13	54.49	2185
C2	60°	16	15.17	3.57	11.02	3610
C2	90°	1047	9.45	1.98	15.31	3660
C2	90°	1049	9.89	18.30	54.59	2225
C3	30°	1021	10.20	2.23	15.37	3718
C3	30°	1022	10.55	4.74	18 50	2792
C3	30°	1023	10.06	19.34	54.84	2200
C3	60°	1027	10.20	2.44	15.02	3490
C3	60°	1026	10.78	4.80	17.33	2741
C3	60°	1025	10.00	19.09	55.74	2216
C3	60°	18	15.48	3.87	10.47	3430

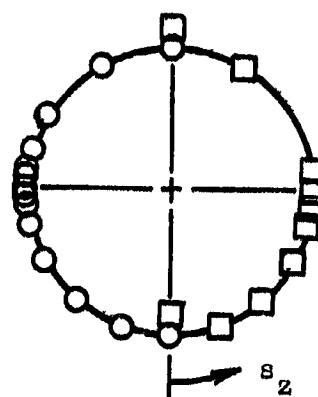
Table 2 Cont.

Conf	$\alpha$	Run No.	$M_\infty$	$Re_\infty/ft$ $\times 10^{-6}$	$P_{t2}$ (psia)	$T_t$ (°R)
C3	90°	1028	10.37	2.53	14.83	3443
C3	90°	1032	9.95	22.53	50.07	1861
C4	30°	1012	10.31	2.53	14.98	3450
C4	30°	1011	10.70	4.85	17.42	2710
C4	30°	1010	10.15	20.21	55.52	2185
C4	30°	8	15.35	3.98	10.79	3395
C4	60°	1015	10.43	2.29	14.52	3630
C4	60°	1016	10.72	4.75	17.20	2730
C4	60°	1017	10.13	20.77	53.19	2082
C4	60°	5	15.35	3.87	10.90	3470
C4	90°	1020	10.17	2.29	15.23	3630
C4	90°	1019	10.25	21.18	51.97	2063
C4	90°	13	15.13	3.75	11.29	3550





$$W_b = 1.5''$$

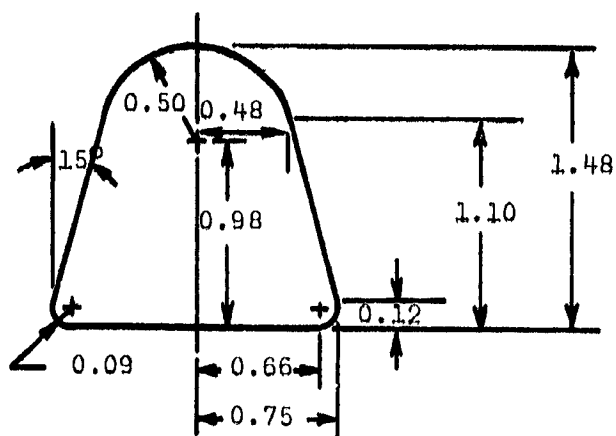


○ Thermocouples			
$x_{ic}$	$\frac{s_z}{0.5W_b}$	$x_{ic}$	$\frac{s_z}{0.5W_b}$
1.25	0.0000	1.25	1.702
1.25	0.349	1.25	1.832
1.25	0.698	1.25	2.094
1.25	1.047	1.25	2.618
1.25	1.309	1.25	3.142
1.25	1.440	.50	0.000
1.25	1.504	.50	3.142
1.25	1.570	1.75	0.000
1.25	1.635	1.75	3.142

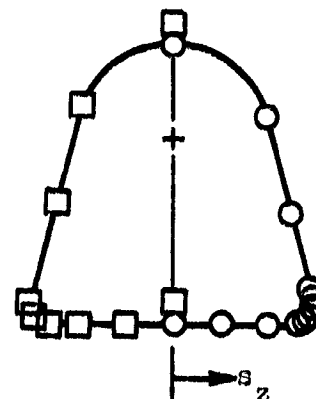
□ Pressure Orifices			
$x_{ic}$	$\frac{s_z}{0.5W_b}$	$x_{ic}$	$\frac{s_z}{0.5W_b}$
1.05	0.000	1.25	2.618
1.25	0.349	1.05	3.142
1.25	0.698		
1.25	1.047		
1.25	1.309		
1.25	1.440		
1.25	1.570		
1.25	1.702		

(a) Configuration C1

Figure 1. Cylindrical cross-sections with instrumentation locations.



$$W_b = 1.5''$$



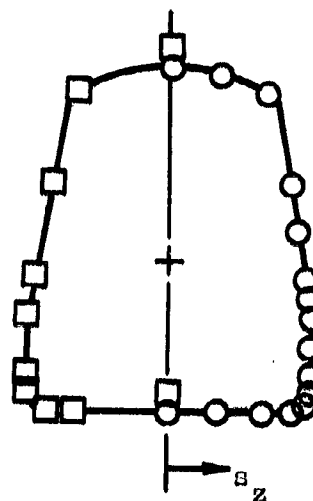
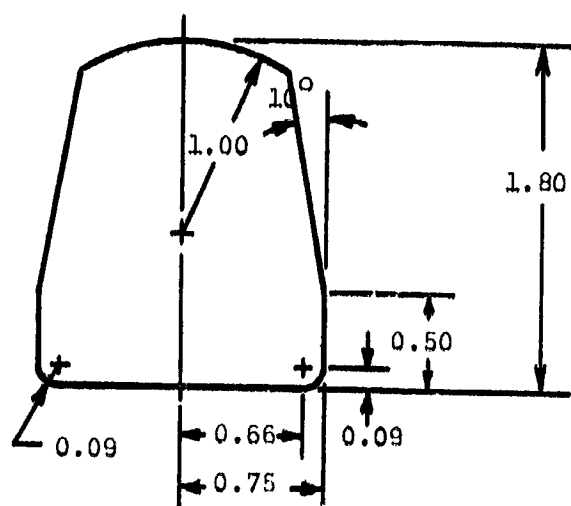
Note: all dimensions in inches

○ Thermocouples			
$x_{ic}$	$\frac{s_z}{0.5W_b}$	$x_{ic}$	$\frac{s_z}{0.5W_b}$
1.25	0.000	1.25	1.744
1.25	0.333	1.25	2.464
1.25	0.667	1.25	3.343
1.25	0.875	.50	0.000
1.45	0.973	.50	0.875
1.05	1.006	.50	1.006
1.25	1.071	.50	3.343
1.45	1.104	1.75	0.000
1.05	1.138	1.75	1.071

□ Orifice Pressures			
$x_{ic}$	$\frac{s_z}{0.5W_b}$	$x_{ic}$	$\frac{s_z}{0.5W_b}$
1.05	0.000	1.05	3.343
1.25	0.333	.50	1.104
1.25	0.667		
1.25	0.875		
1.25	1.006		
1.45	1.104		
1.25	1.744		
1.25	2.464		

(b) Configuration C2

Figure 1. Continued.



$$W_b = 1.5''$$

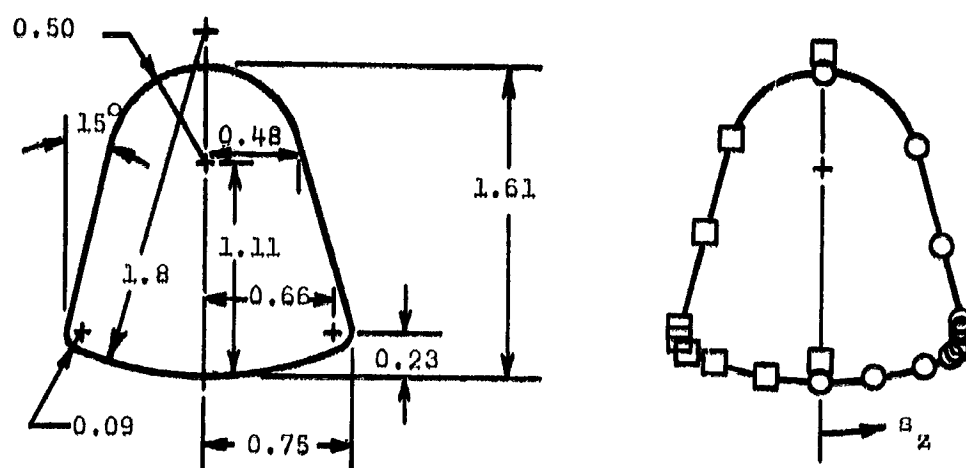
Note: all dimensions in inches

○ Thermocouples			
$x_{ic}$	$\frac{s_z}{0.5W_b}$	$x_{ic}$	$\frac{s_z}{0.5W_b}$
1.25	0.000	1.25	1.738
1.25	0.333	1.25	1.872
1.25	0.667	1.25	2.205
1.25	0.875	1.25	2.539
1.25	0.973	1.25	3.165
1.25	1.071	1.25	3.515
1.25	1.204	1.25	3.864
1.25	1.405	1.75	0.000
1.25	1.605	1.75	1.071

□ Pressure Orifices			
$x_{ic}$	$\frac{s_z}{0.5W_b}$	$x_{ic}$	$\frac{s_z}{0.5W_b}$
1.05	0.000	1.25	2.534
1.25	0.667	1.25	3.165
1.25	0.875	1.05	3.864
1.45	1.071		
1.25	1.204		
1.25	1.605		
1.25	1.872		

(c) Configuration C3

Figure 1. Continued.



$$W_b = 1.5''$$

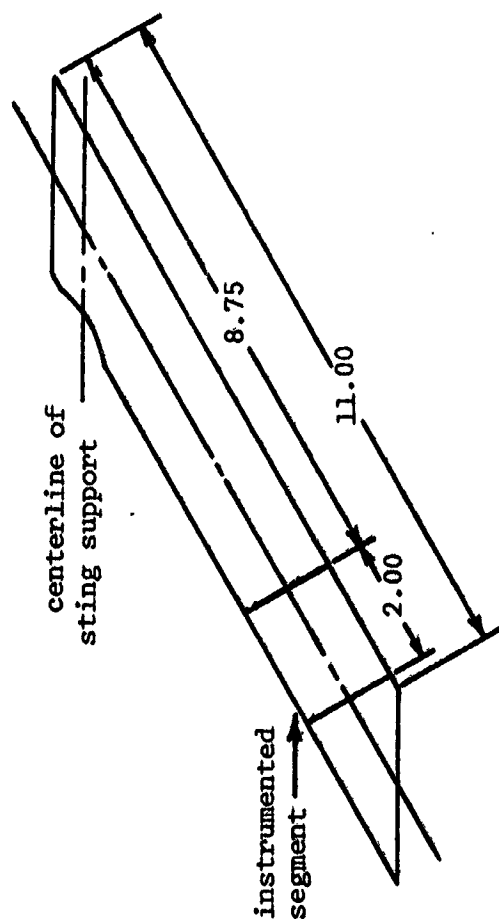
Note: all dimensions in inches

○ Thermocouple			
$x_{ic}$	$\frac{s_z}{0.5W_b}$	$x_{ic}$	$\frac{s_z}{0.5W_b}$
1.25	0.000	1.25	1.766
1.25	0.378	1.25	2.486
1.25	0.755	1.25	3.365
1.25	0.946	0.5	0.000
1.45	0.995	0.5	0.946
1.05	1.028	0.5	1.126
1.25	1.093	0.5	3.365
1.45	1.126	1.75	0.000
1.05	1.160	1.75	1.093

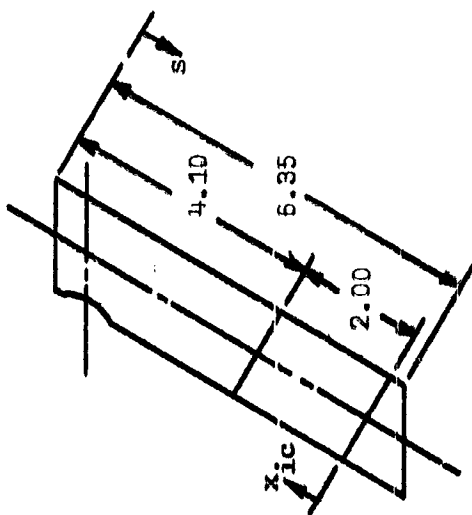
□ Pressure Orifice			
$x_{ic}$	$\frac{s_z}{0.5W_b}$	$x_{ic}$	$\frac{s_z}{0.5W_b}$
1.05	0.000	1.05	3.365
1.25	0.378	.50	1.126
1.25	0.755		
1.25	0.946		
1.05	1.028		
1.45	1.126		
1.25	1.766		
1.25	2.486		

(d) Configuration C4

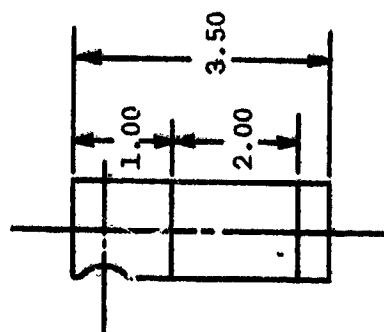
Figure 1. Concluded.



(a)  $\alpha = 30^\circ$  configuration



(b)  $\alpha = 60^\circ$  configuration



(c)  $\alpha = 90^\circ$  configuration

Note: all dimensions in inches

Figure 2. Sketch of "infinite" cylinder models indicating location of instrumented section as a function of the angle-of-attack.

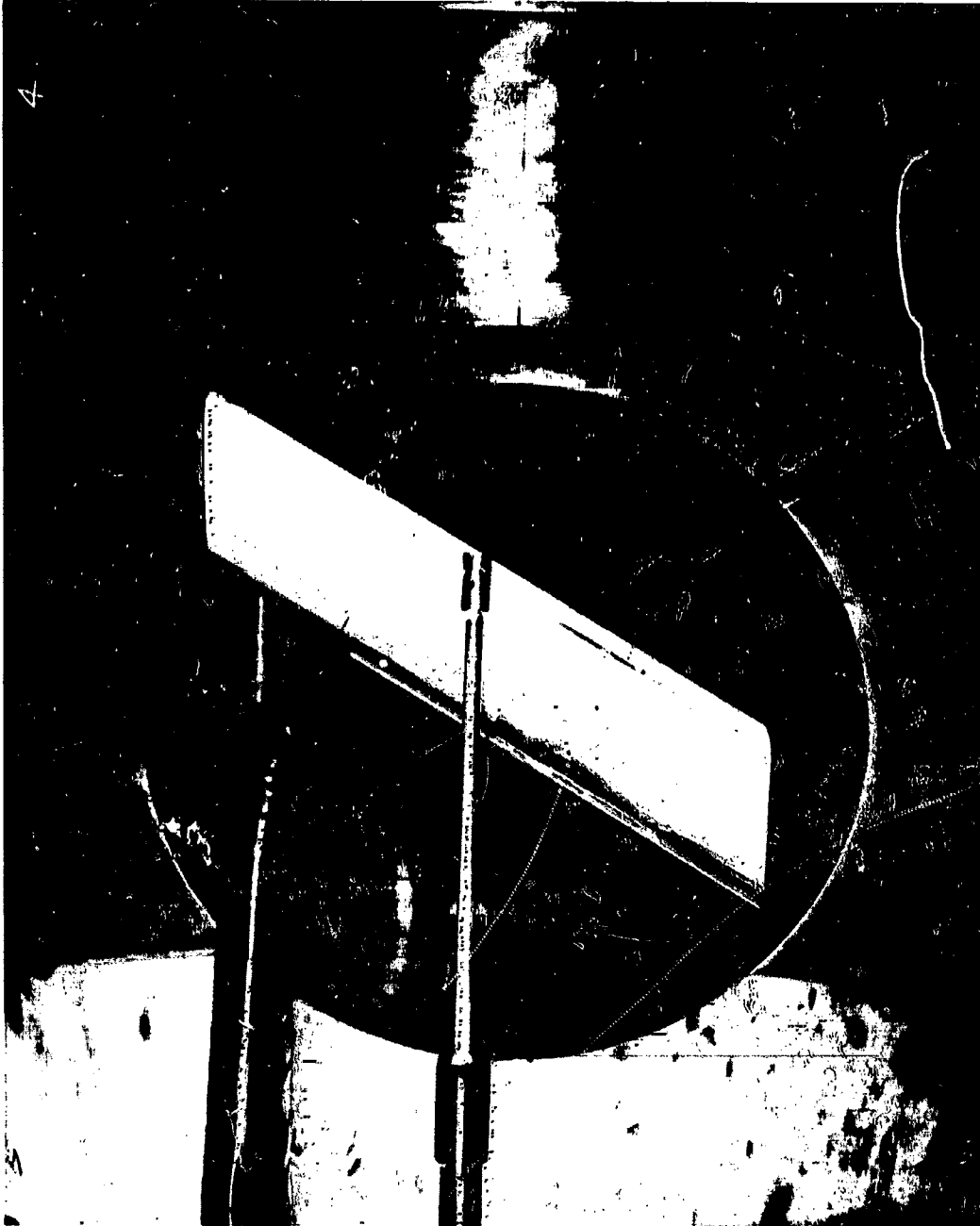
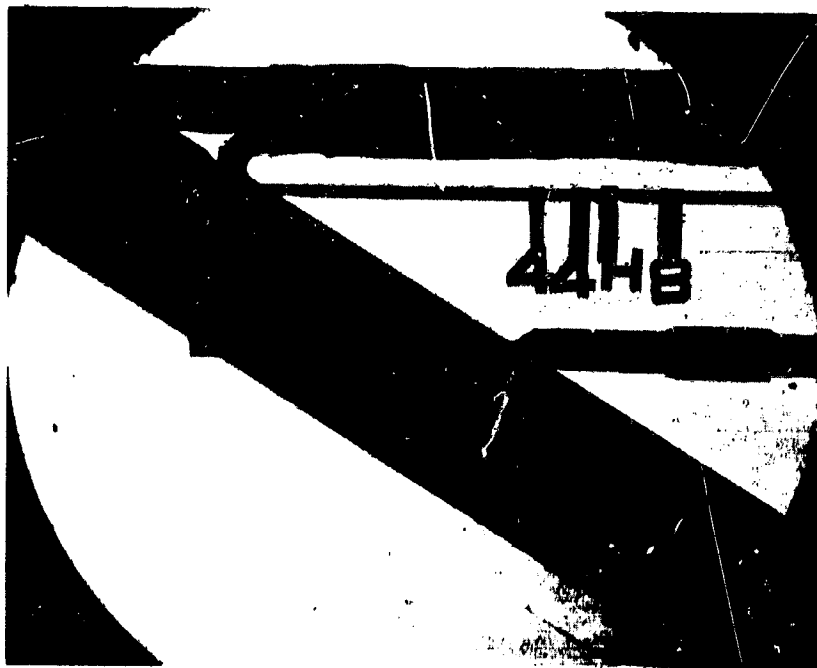


Figure 3. Typical model installation for an "infinite" cylinder in the Hypervelocity Wind Tunnel.



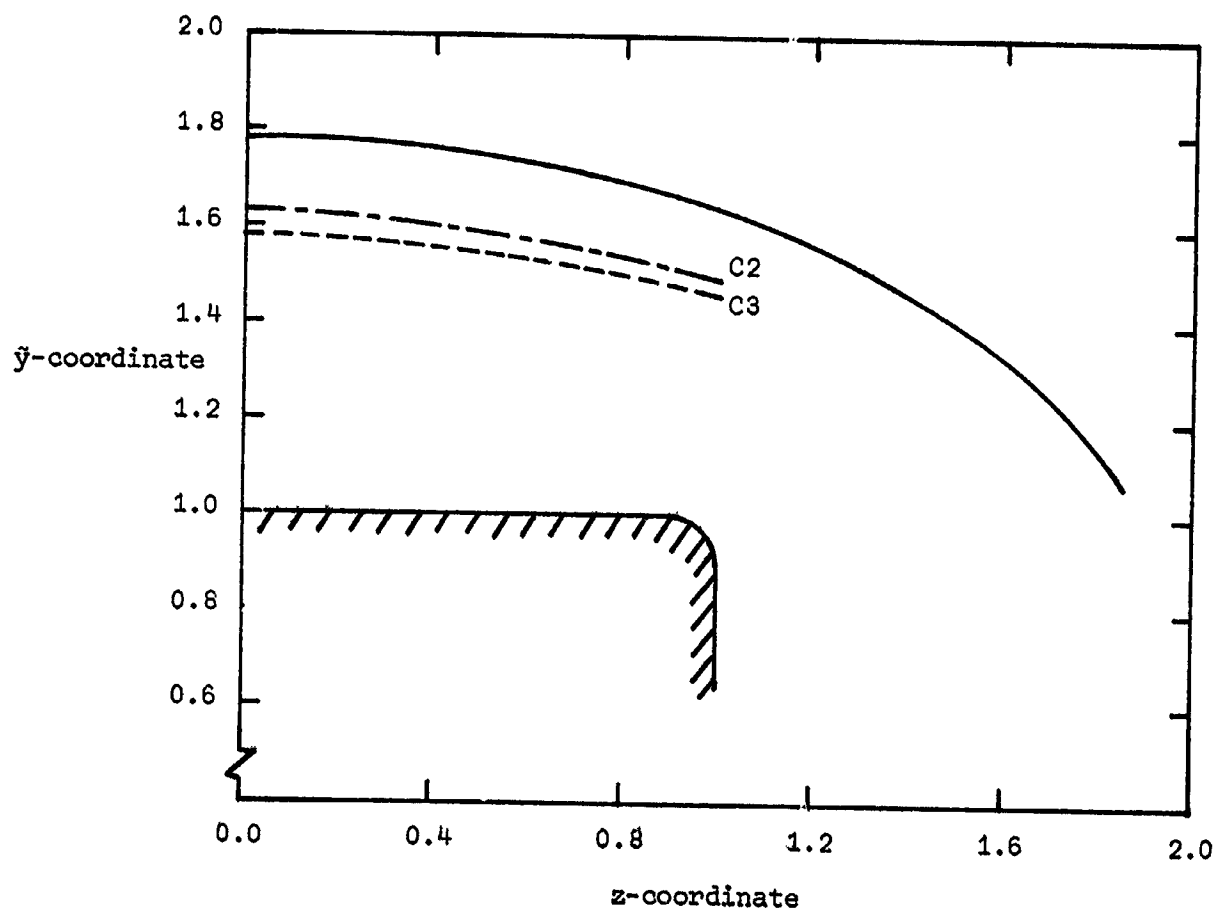
(a)  $M_\infty = 15.35$ ,  $Re_\infty/ft = 3.98 \times 10^6$ , (Run 8)



(b)  $M_\infty = 10.15$ ,  $Re_\infty/ft = 20.21 \times 10^6$ , (Run 1010)

Figure 4. - Effect of model degradation on the flow-field of an infinite cylinder at angle-of-attack.

- shock wave calculated using numerical technique of f. 10 for  $M_\infty=8$   
 - - shock wave observed for Configuration C2 for  $M_\infty=8$   
 - - - shock wave observed for Configuration C3 for  $M_\infty=10$

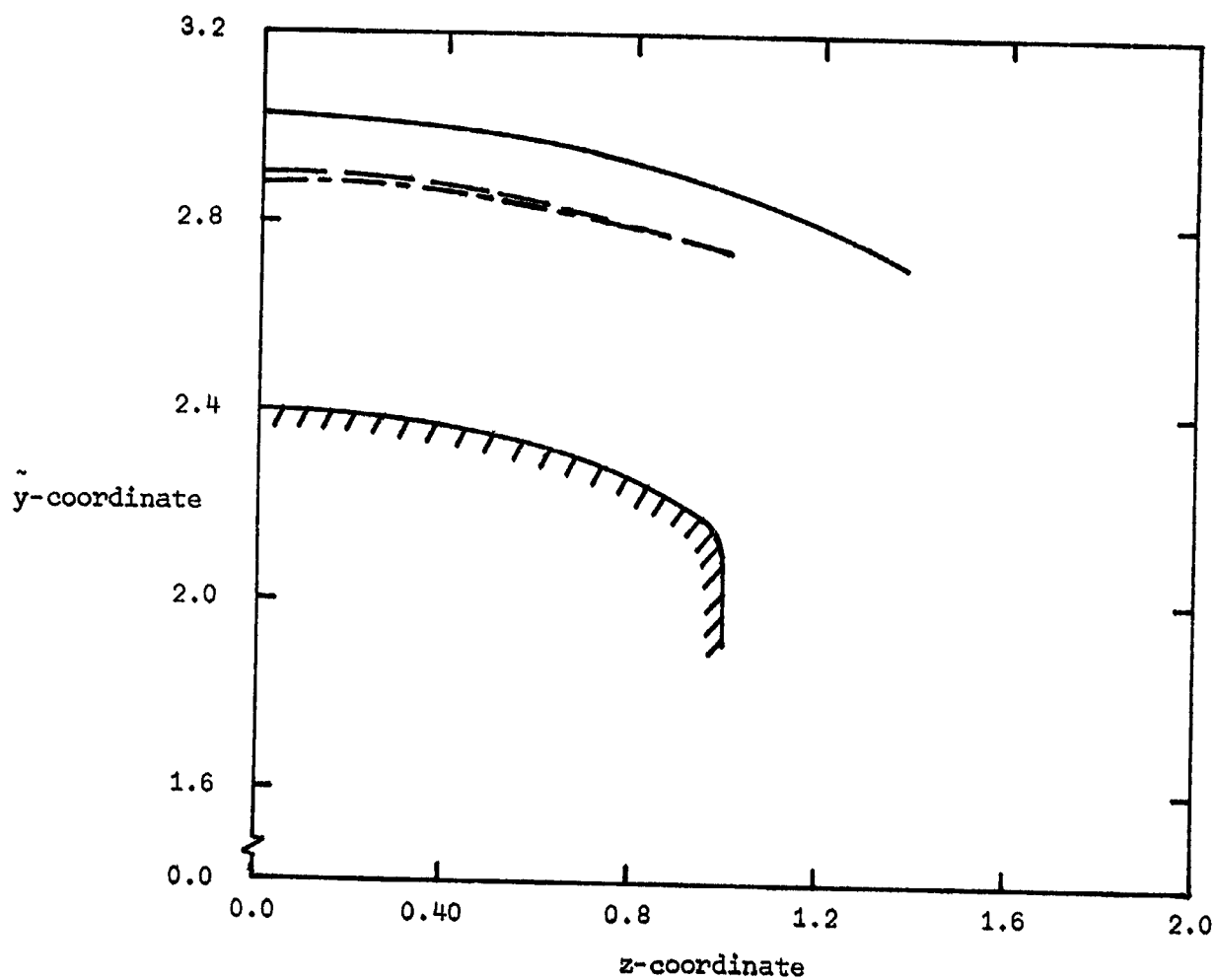


(a) Configurations C2 and C3

Figure 5. - Comparison of experimental shock wave with theoretical shock wave for infinite cylinder at an angle-of-attack of  $90^\circ$ .



- shock wave calculated using numerical technique (ref. 10) for  $M_\infty=15$
- - shock wave observed for Configuration C4 for  $M_\infty=15$
- - shock wave observed for Configuration C4 for  $M_\infty=10$



(b) Configuration C4

Figure 5. - Concluded

Configuration C2

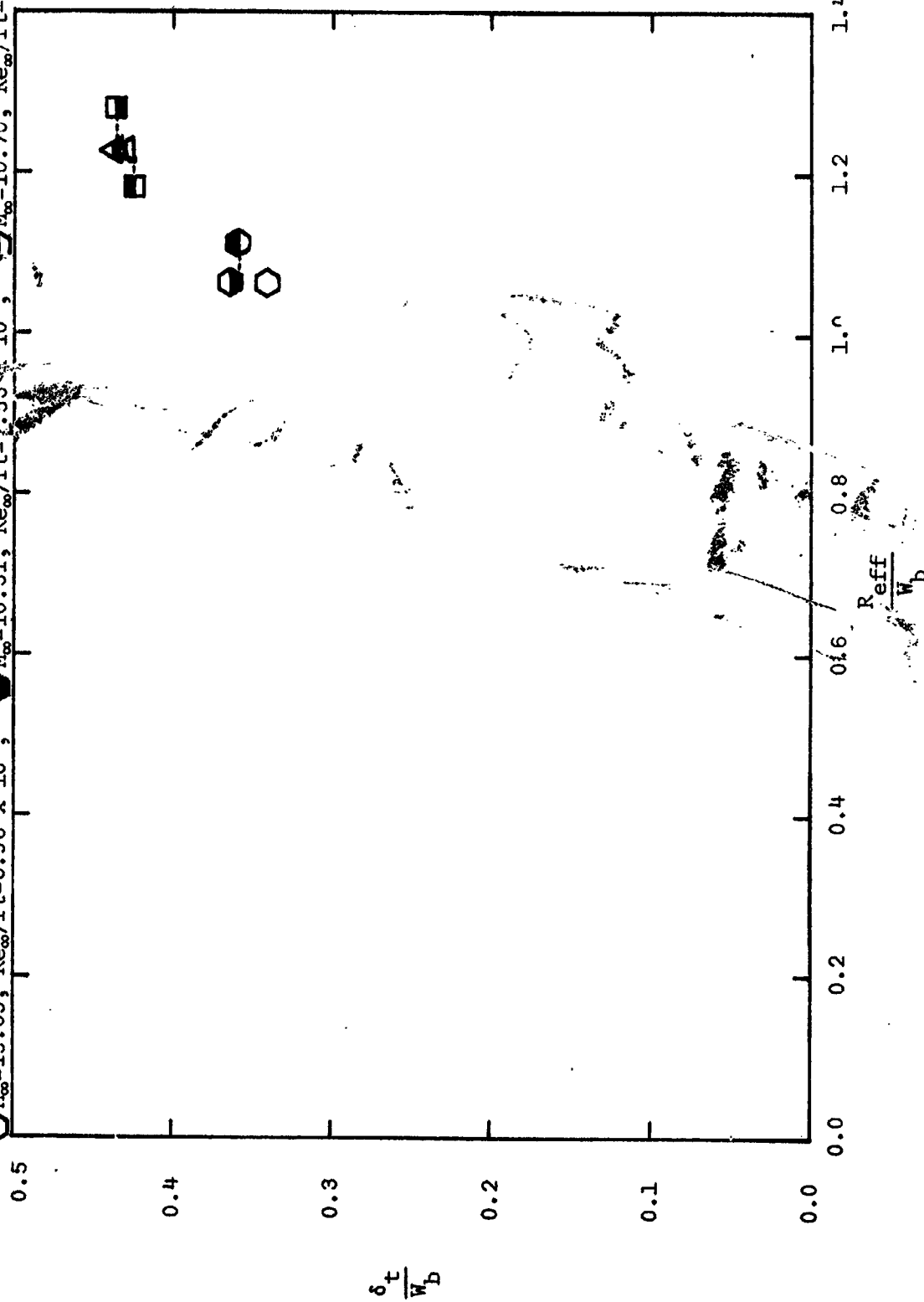
$\blacktriangle M_\infty=10.16, Re_\infty/ft=2.15 \times 10^6$ ;  $\triangle M_\infty=10.43, Re_\infty/ft=4.33 \times 10^6$

Configuration C3

$\blacksquare M_\infty=10.20, Re_\infty/ft=2.23 \times 10^6$ ;  $\square M_\infty=10.55, Re_\infty/ft=4.74 \times 10^6$

Configuration C4

$\circ M_\infty=15.35, Re_\infty/ft=3.98 \times 10^6$ ;  $\odot M_\infty=10.31, Re_\infty/ft=2.53 \times 10^6$ ;  $\ominus M_\infty=10.70, Re_\infty/ft=4.85 \times 10^6$



(a)  $\alpha=30^\circ$   
Figure 6. - Shock stand-off distance in the pitch plane of an infinite cylinder at various angles-of-attack.

Configuration C1

$\bigcirc M_{\infty}=14.98, Re_{\infty}/ft=3.96 \times 10^6; \bigcirc M_{\infty}=10.00, Re_{\infty}/ft=2.17 \times 10^6$

Configuration C2

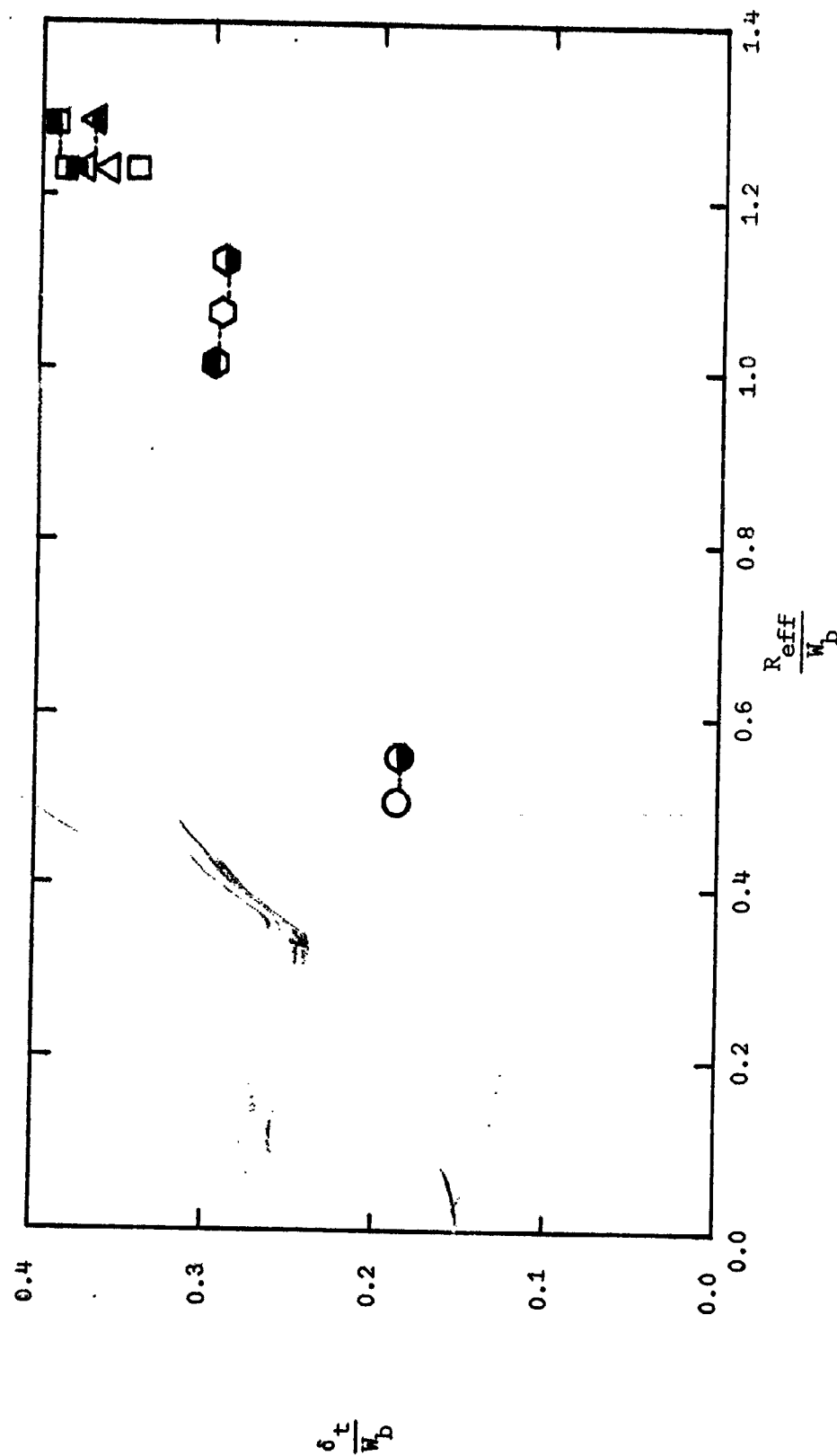
$\triangle M_{\infty}=15.17, Re_{\infty}/ft=3.57 \times 10^6; \triangle M_{\infty}=10.20, Re_{\infty}/ft=2.47 \times 10^6; \triangle M_{\infty}=10.52, Re_{\infty}/ft=4.81 \times 10^6$

Configuration C4

$\bigcirc M_{\infty}=15.35, Re_{\infty}/ft=3.87 \times 10^6; \bigcirc M_{\infty}=10.43, Re_{\infty}/ft=2.29 \times 10^6; \bigcirc M_{\infty}=10.72, Re_{\infty}/ft=4.75 \times 10^6$

Configuration C3

$\square M_{\infty}=15.48, Re_{\infty}/ft=3.87 \times 10^6; \square M_{\infty}=10.20, Re_{\infty}/ft=2.44 \times 10^6; \square M_{\infty}=10.78, Re_{\infty}/ft=4.80 \times 10^6$

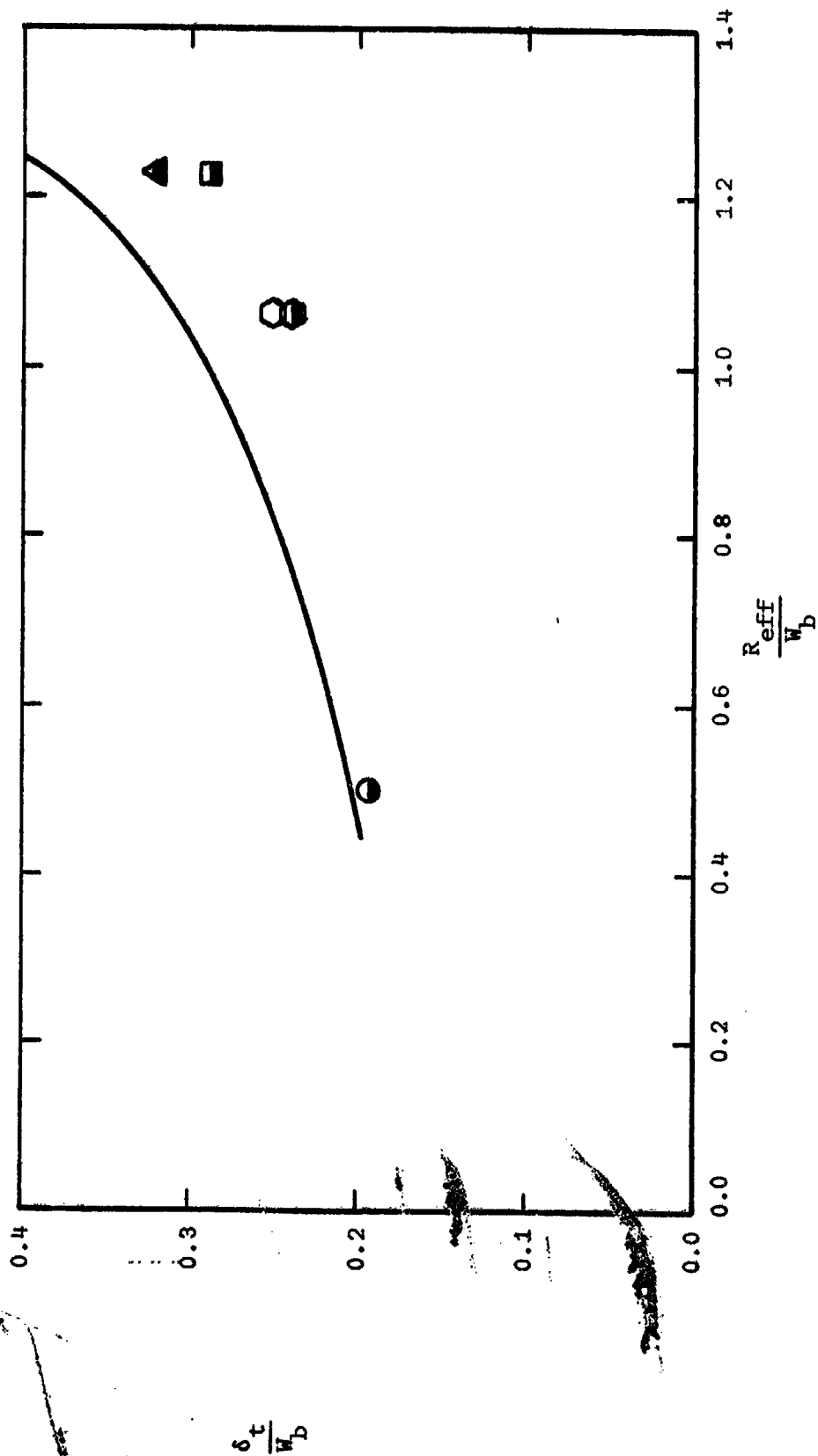


(b)  $\alpha=60^\circ$

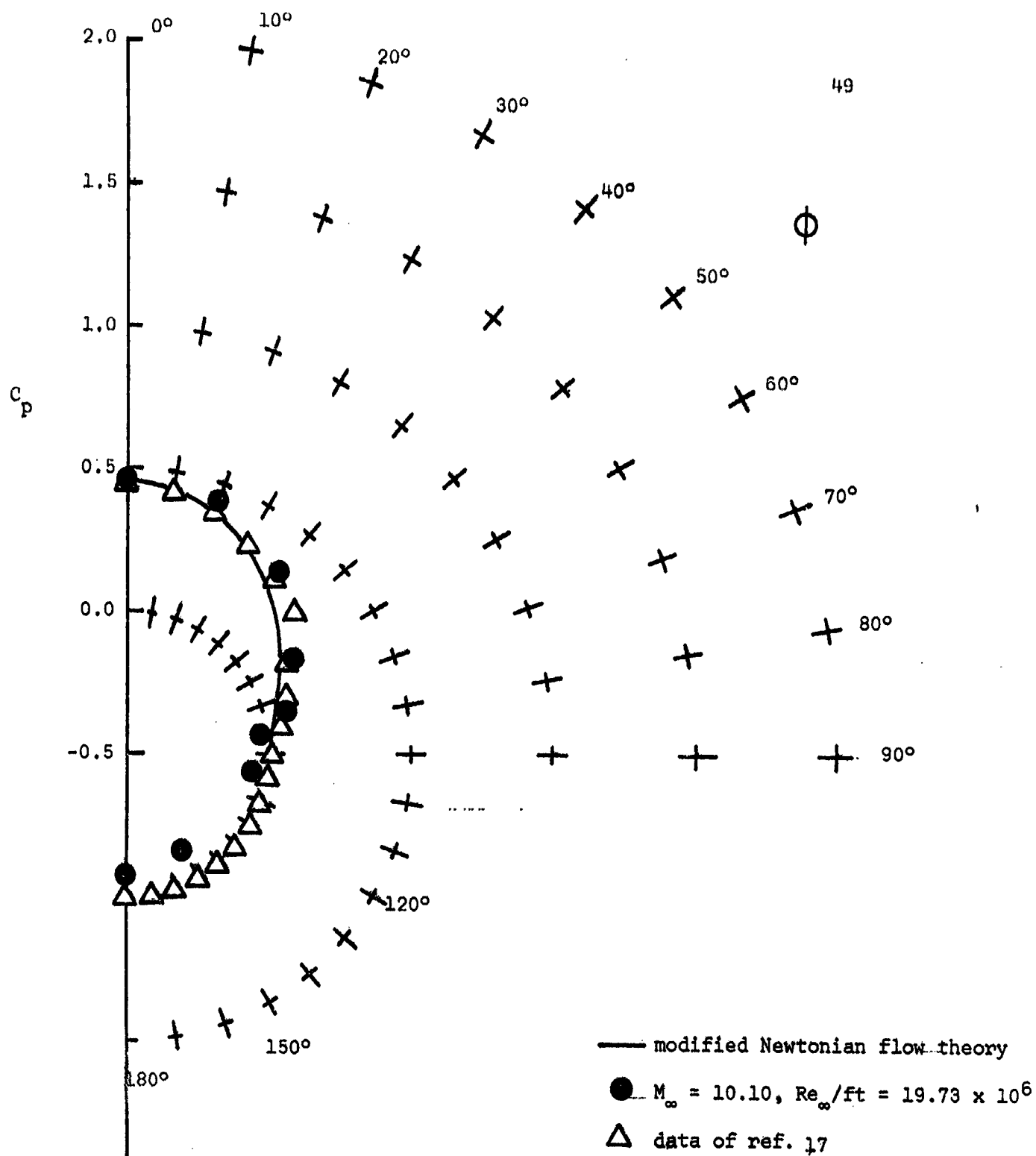
Figure 6. - Continued

— shock wave calculated using numerical technique (ref. 10)

- Configuration C1  $\bullet$   $M_\infty=10.00$ ,  $Re_\infty/ft=2.17 \times 10^6$  Configuration C2  $\blacktriangle$   $M_\infty=9.45$ ,  $Re_\infty/ft=1.98 \times 10^5$   
 Configuration C3  $\blacksquare$   $M_\infty=10.37$ ,  $Re_\infty/ft=2.53 \times 10^6$   
 Configuration C4  $\bullet$   $M_\infty=15.13$ ,  $Re_\infty/ft=3.75 \times 10^6$ ;  $\bullet$   $M_\infty=10.17$ ,  $Re_\infty/ft=2.29 \times 10^6$

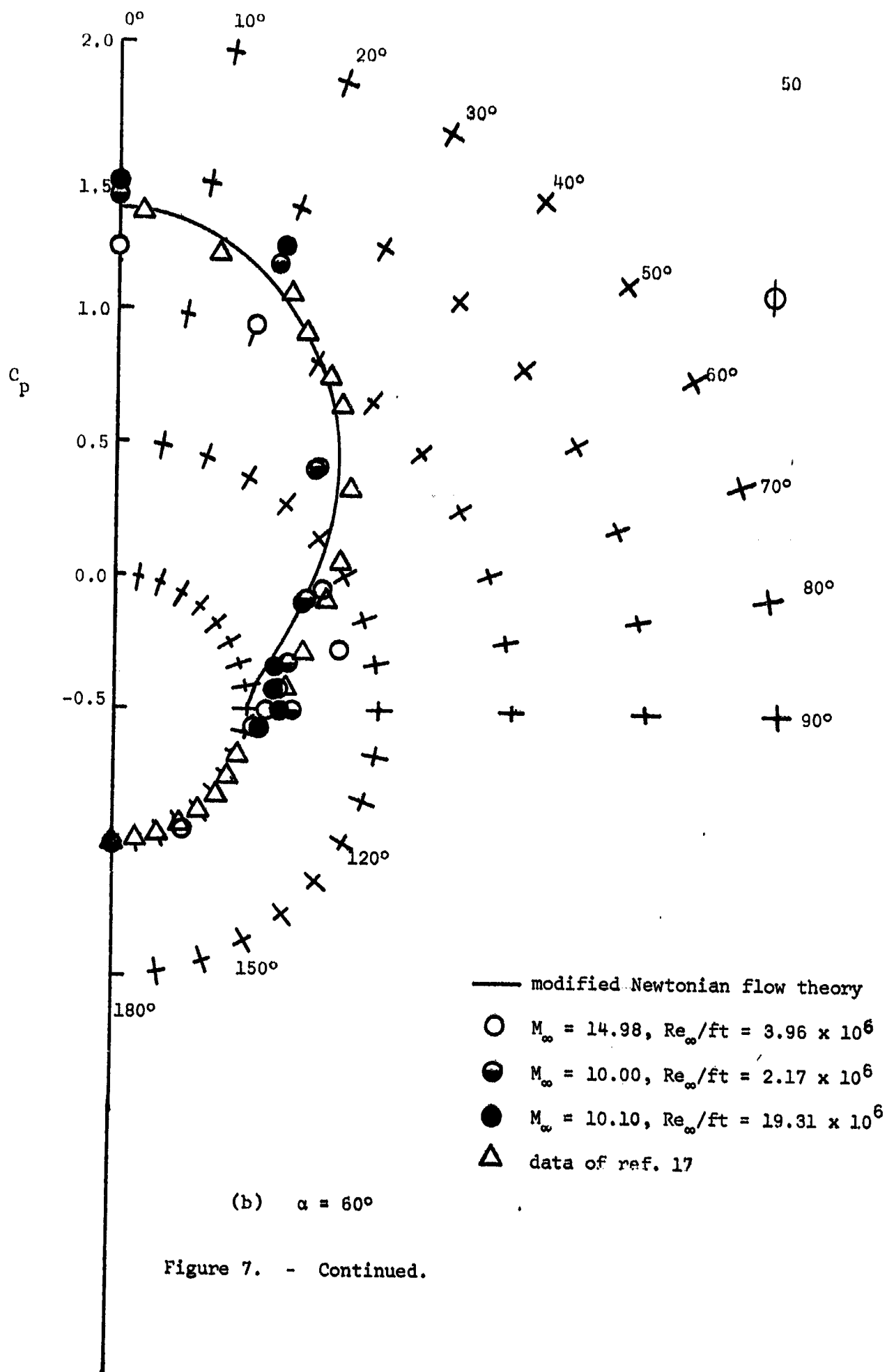


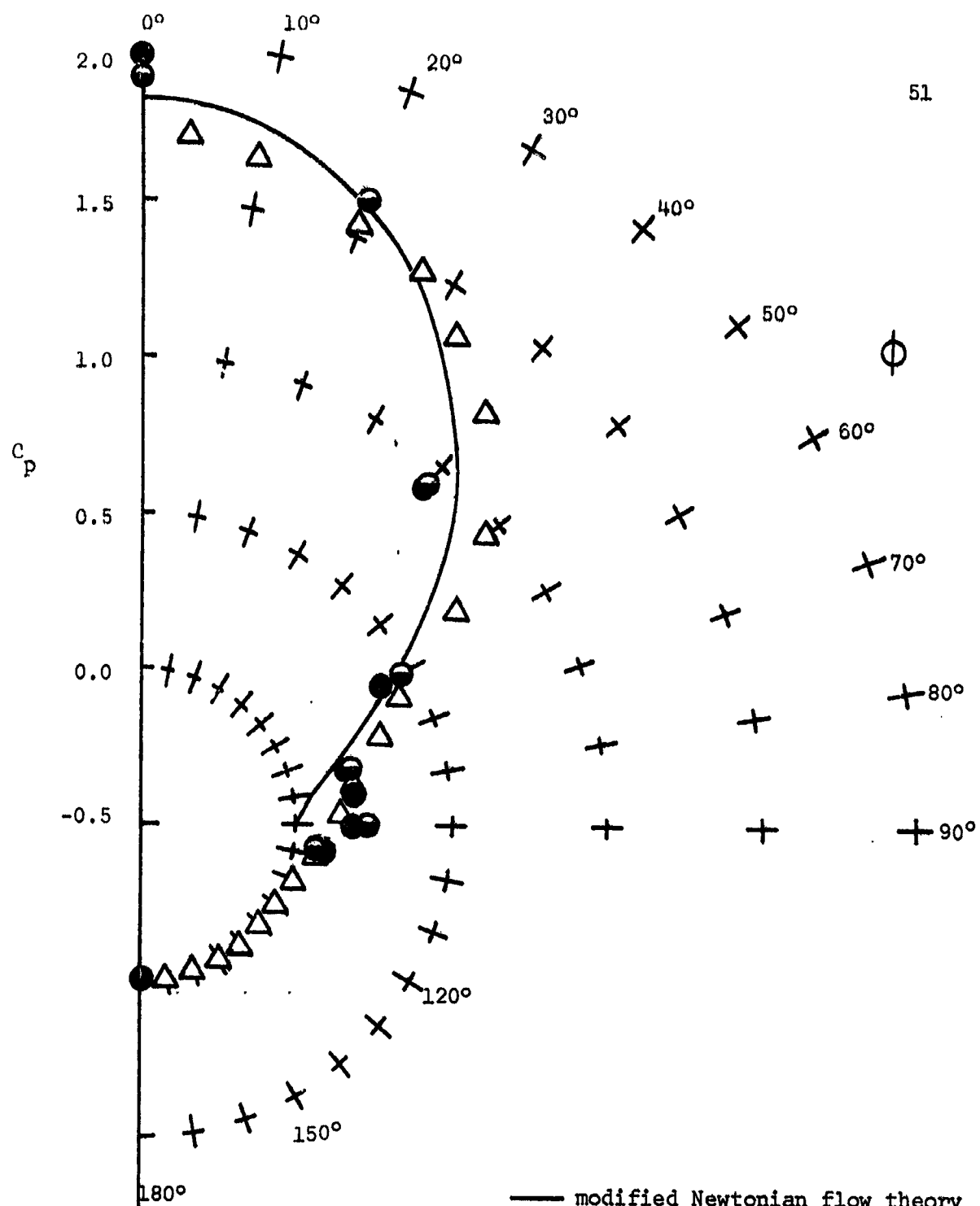
(c)  $\alpha=90^\circ$   
Figure 6. - Concluded



(a)  $\alpha = 30^\circ$

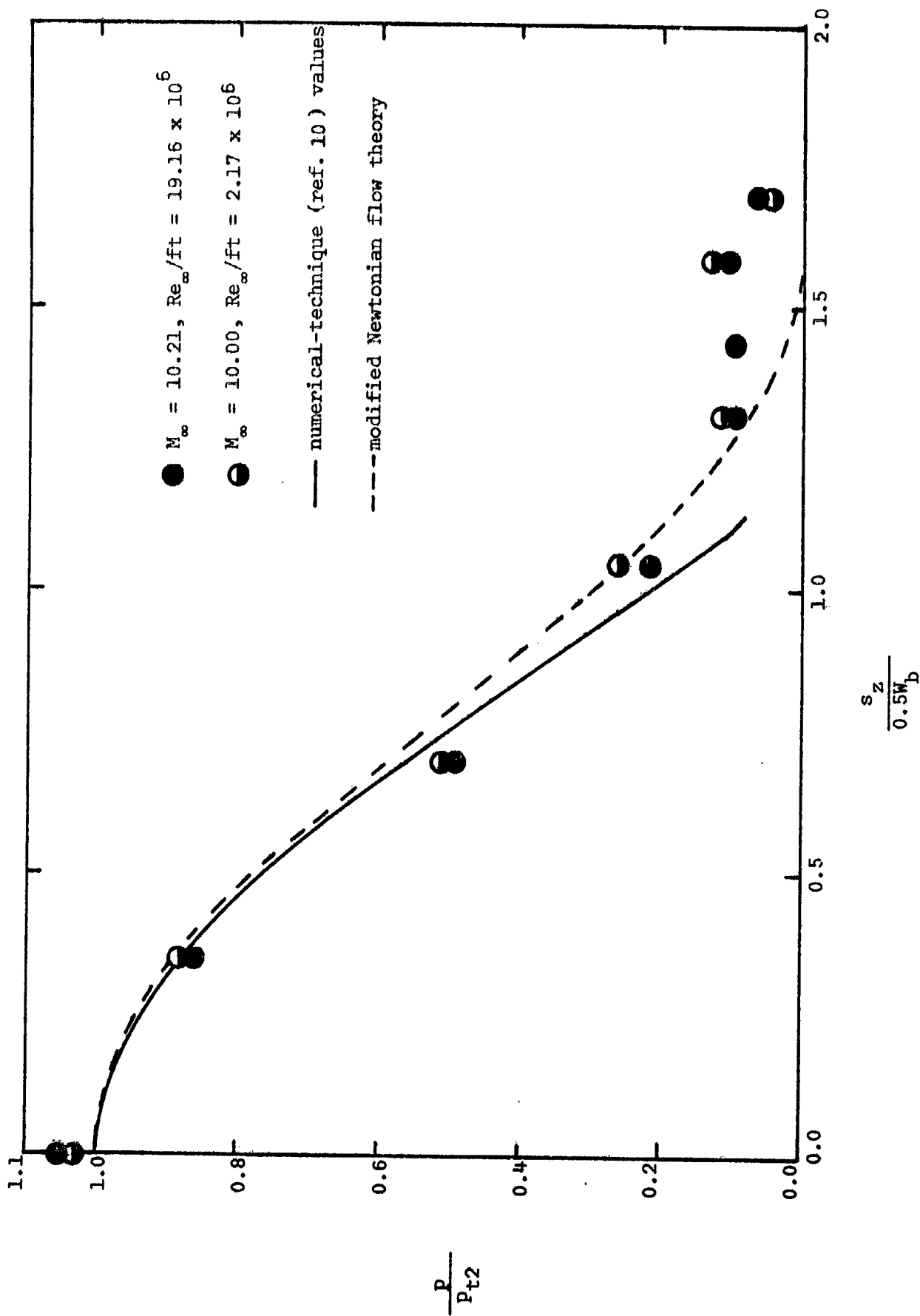
Figure 7. - Circumferential pressure distribution for the right circular cylinder C1 at various angles-of-attack.





(c)  $\alpha = 90^\circ$

Figure 7. - Concluded.



(a) Configuration C1

Figure 8. - Comparison of the measured and the theoretical circumferential pressure distributions for an angle-of-attack of  $90^\circ$ .



## Data for Configuration 2

▲  $M_\infty=9.45$ ,  $Re_\infty/ft=1.98 \times 10^6$

▲  $M_\infty=9.89$ ,  $Re_\infty/ft=18.30 \times 10^6$

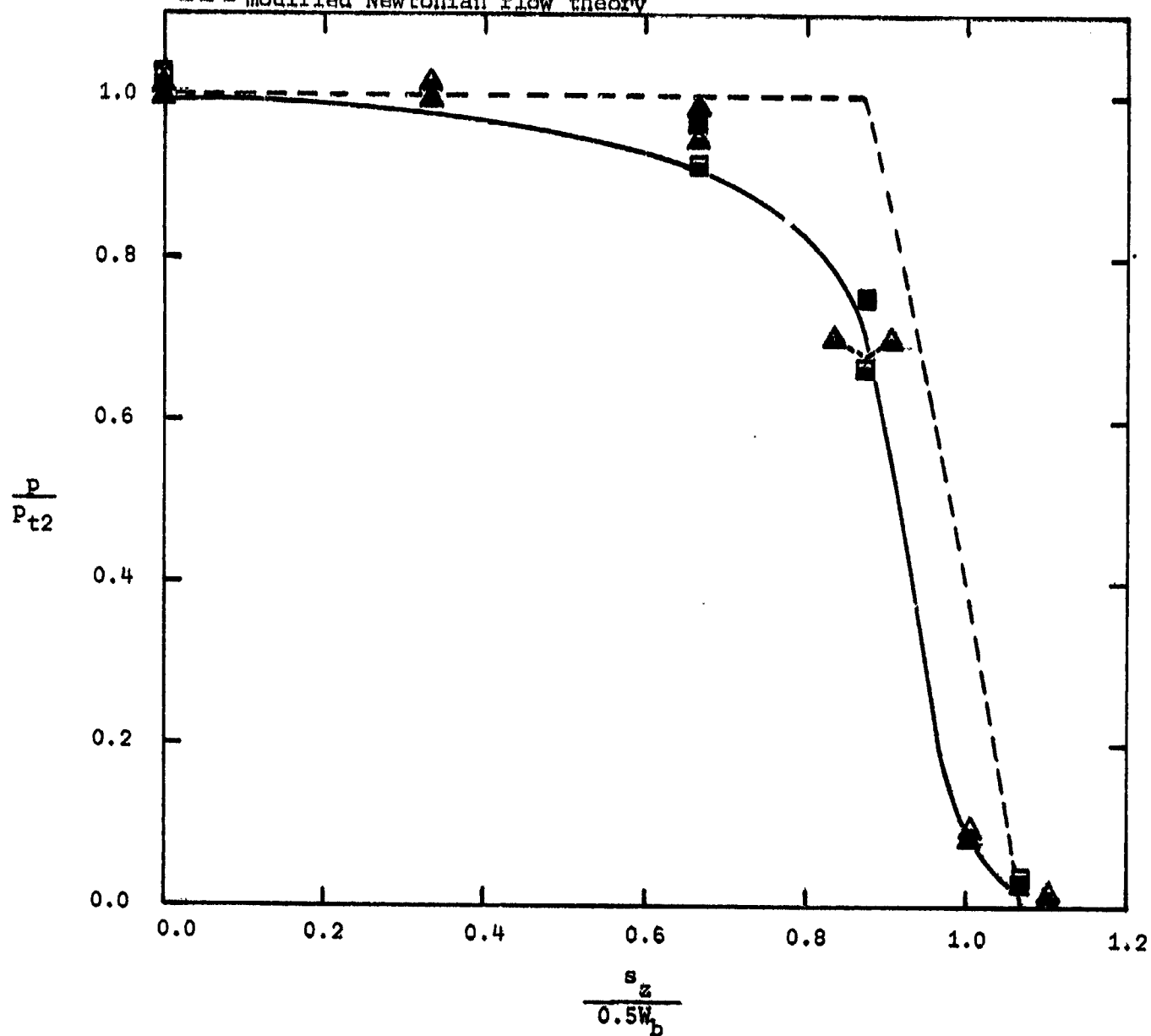
## Data for Configuration 3

■  $M_\infty=10.37$ ,  $Re_\infty/ft=2.53 \times 10^6$

■  $M_\infty=9.95$ ,  $Re_\infty/ft=22.53 \times 10^6$

— numerical technique (ref. 10) values

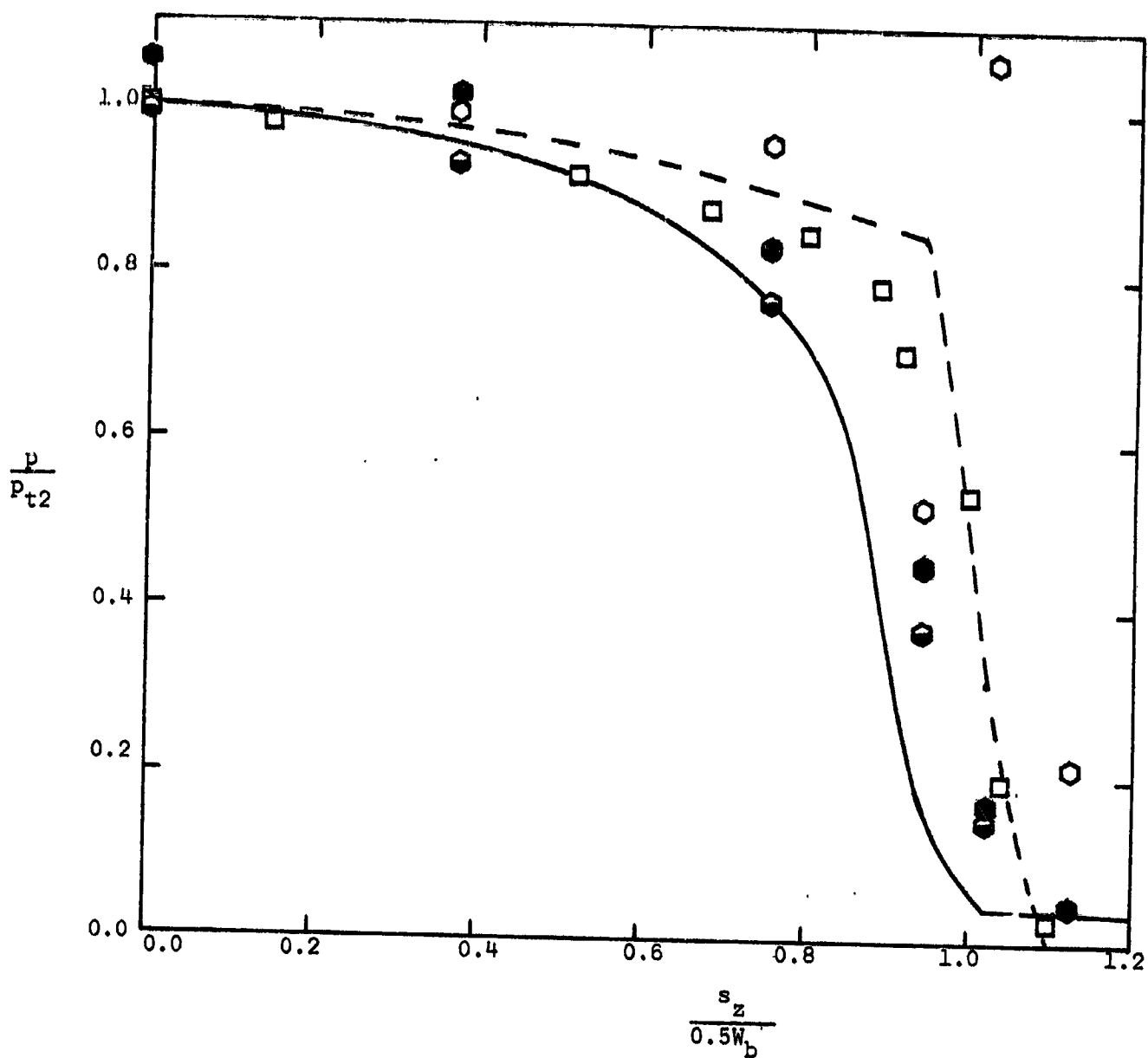
- - - modified Newtonian flow theory



(b) Configurations C2 and C3

Figure 8. - Continued

- $M_\infty = 15.13$ ,  $Re_\infty/ft = 3.75 \times 10^6$
- $M_\infty = 10.17$ ,  $Re_\infty/ft = 2.29 \times 10^6$
- $M_\infty = 10.25$ ,  $Re_\infty/ft = 21.18 \times 10^6$
- data of ref. 19 (for an axisymmetric body)
- numerical technique (ref. 10) values
- modified Newtonian flow theory



(c) Configuration C4

Figure 8. - Concluded.

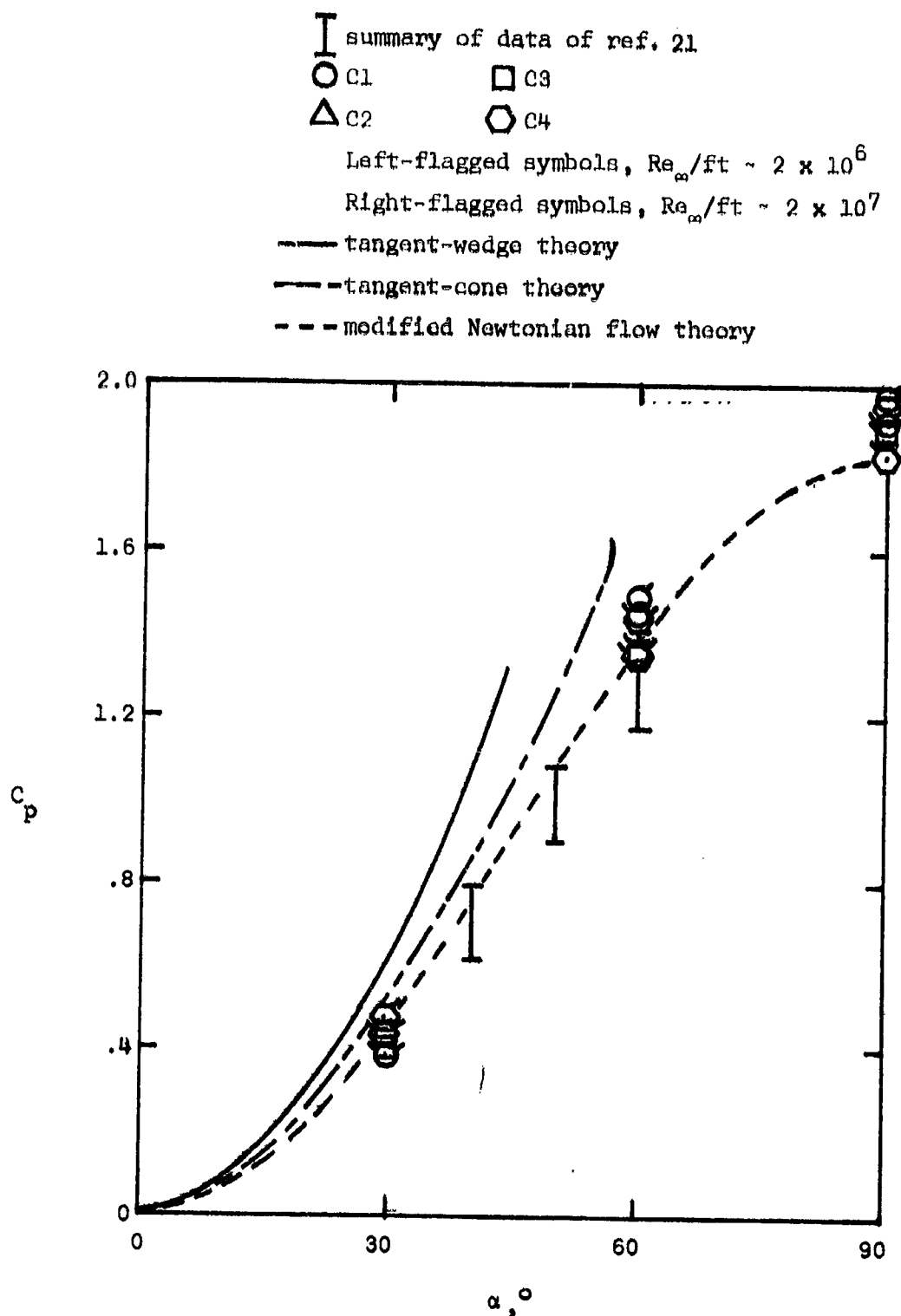
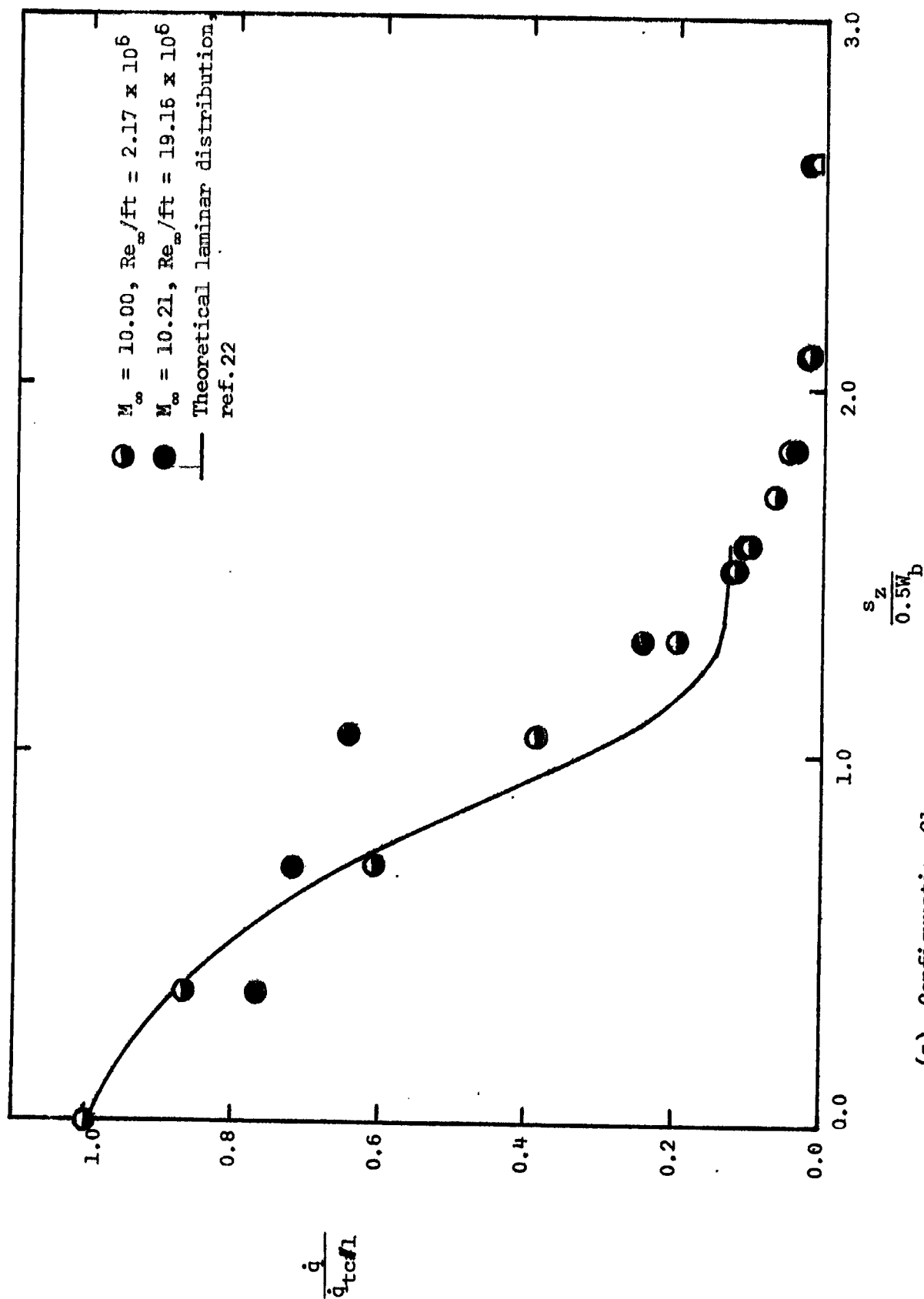


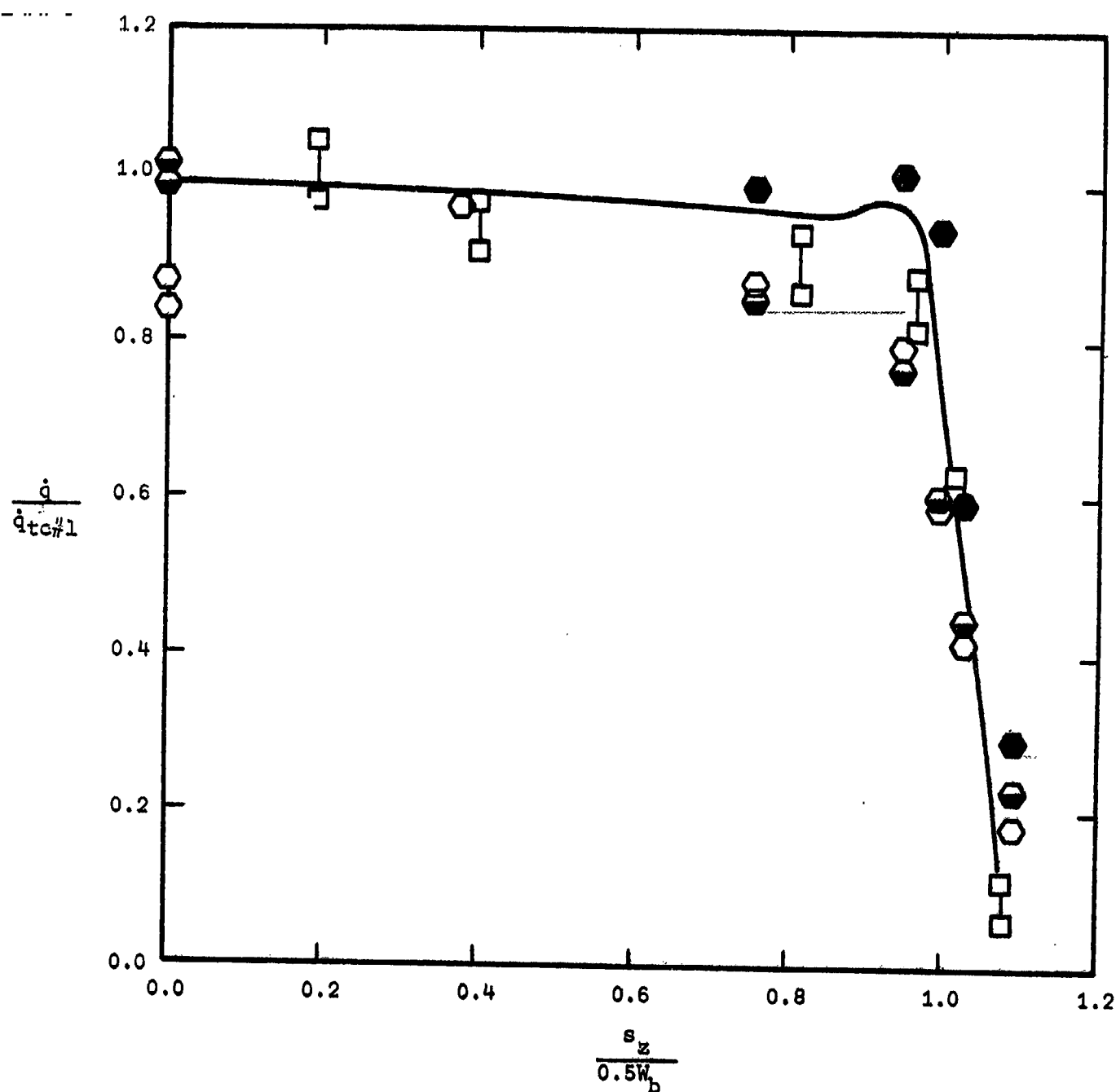
Figure 9. - Pressure measurements from the plane-of-symmetry (i.e., windward-most ray) as a function of the angle-of-attack.



(a) Configuration C1

Figure 10. - Comparison of the measured and the theoretical circumferential heat-transfer distribution for an angle-of-attack of  $90^\circ$ .

- $\circ$   $M_\infty=15.13$ ,  $Re_\infty/ft=3.75 \times 10^6$   
 $\bullet$   $M_\infty=10.17$ ,  $Re_\infty/ft=2.29 \times 10^6$   
 $\bullet$   $M_\infty=10.25$ ,  $Re_\infty/ft=21.18 \times 10^6$   
 $\square$  data of ref. 19 (for an axisymmetric body)  
 — theoretical laminar distribution, ref. 22



(b) Configuration C4

Figure 10. - Concluded.

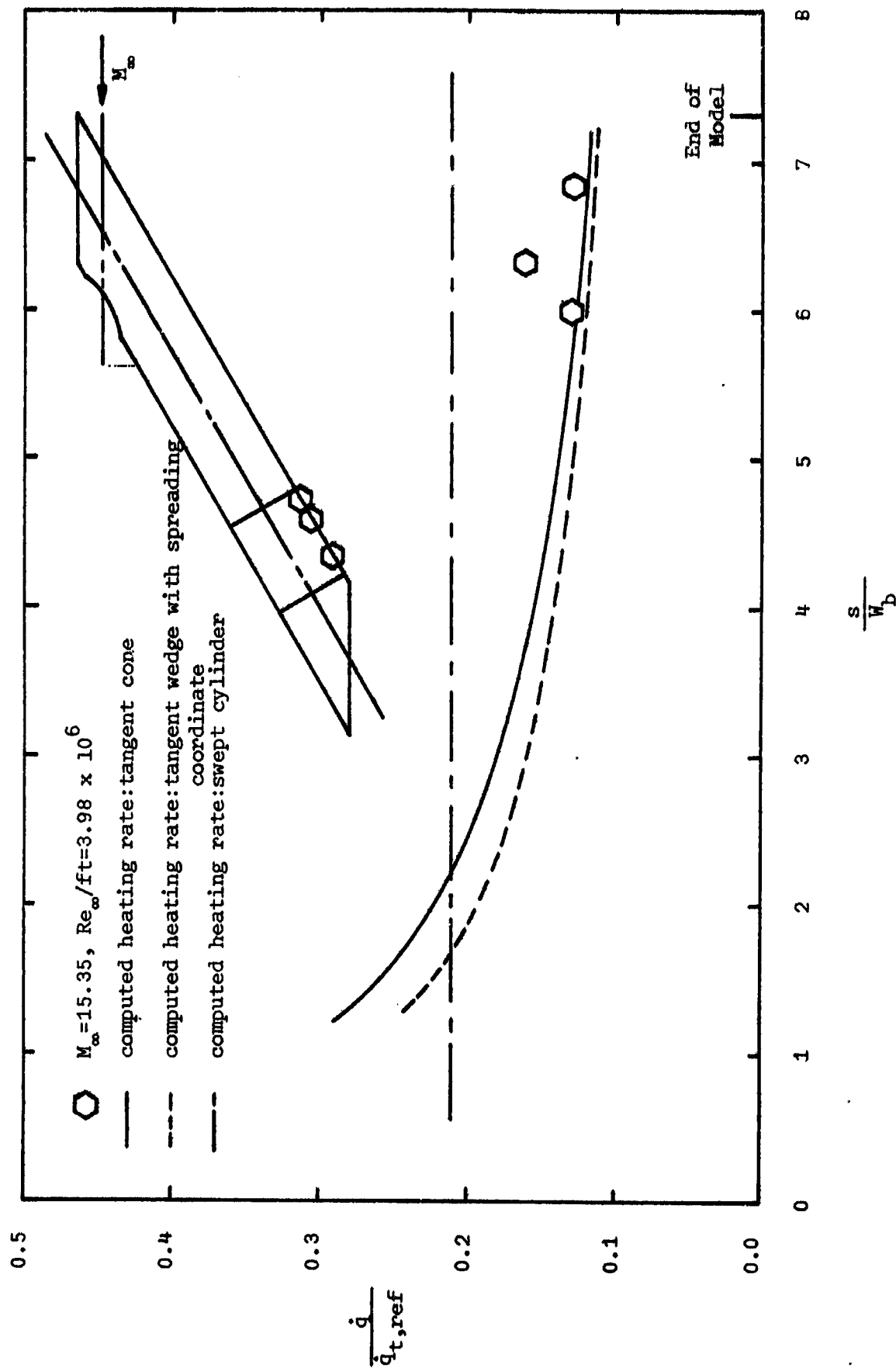
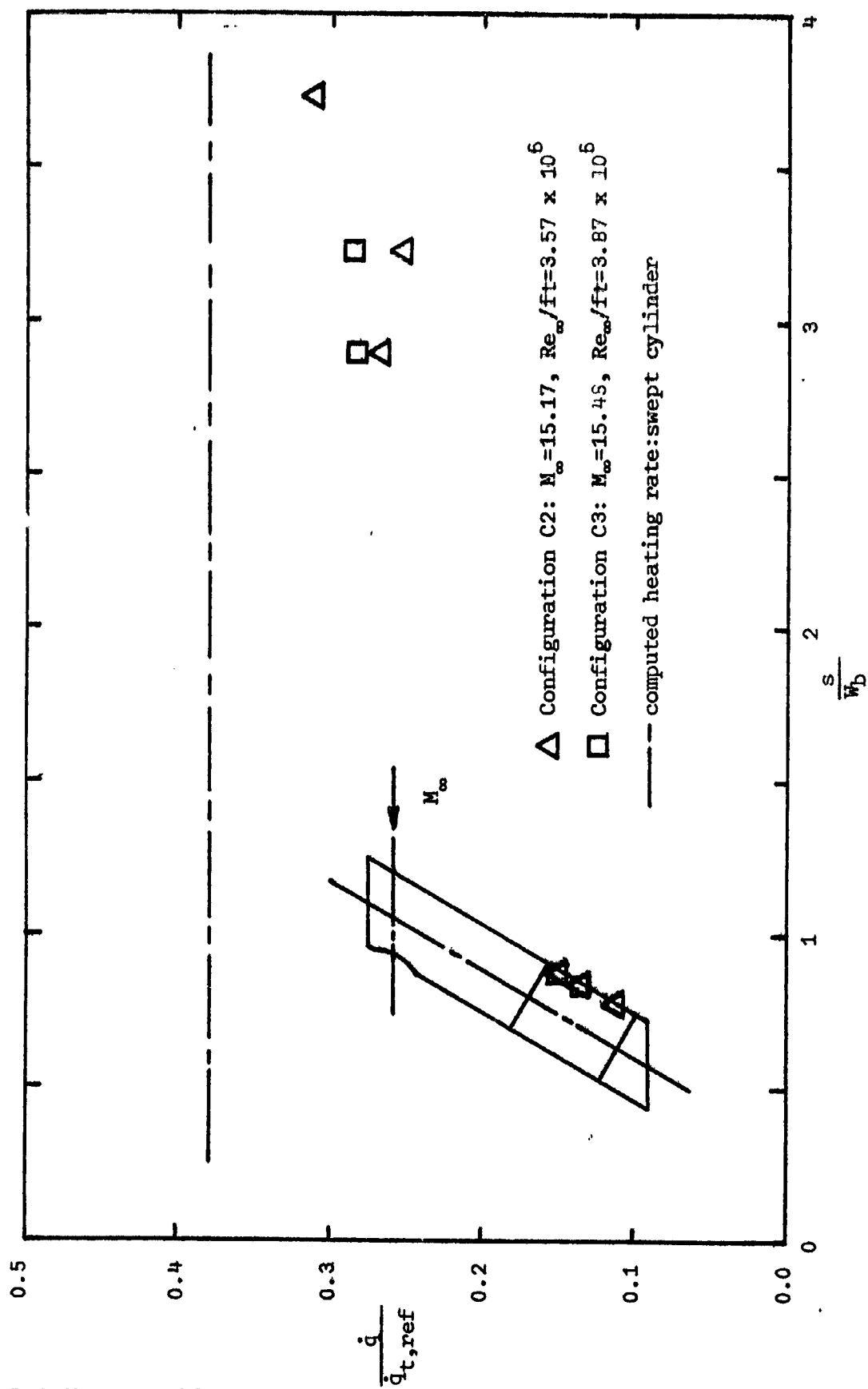


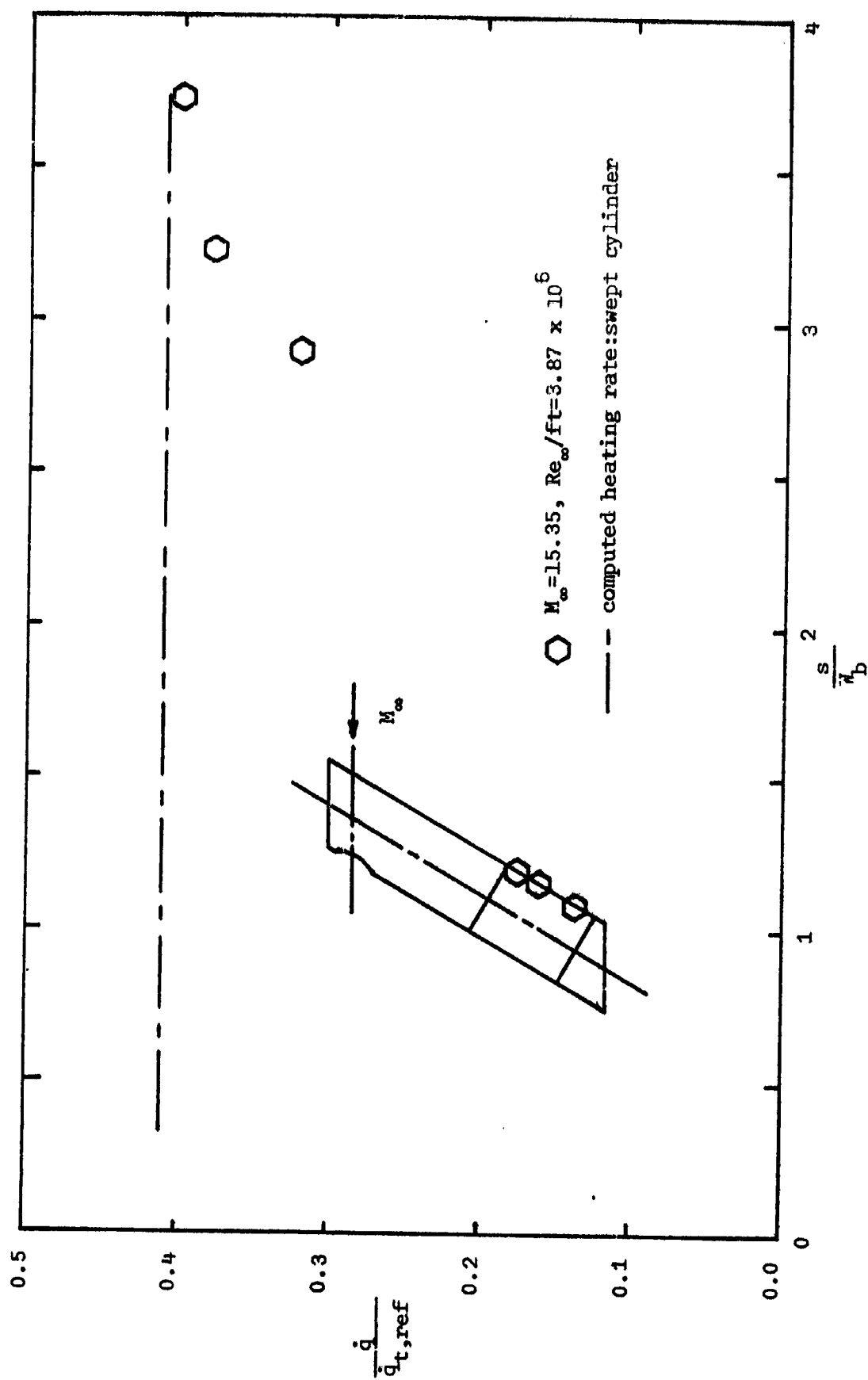
Figure 11. - Heat-transfer-rate "distribution" in the plane of symmetry for an infinite cylinder, configuration C4, at  $\alpha=30$



(a) Configurations C2 and C3

Figure 12. - The heat-transfer-rate "distribution" in the plane

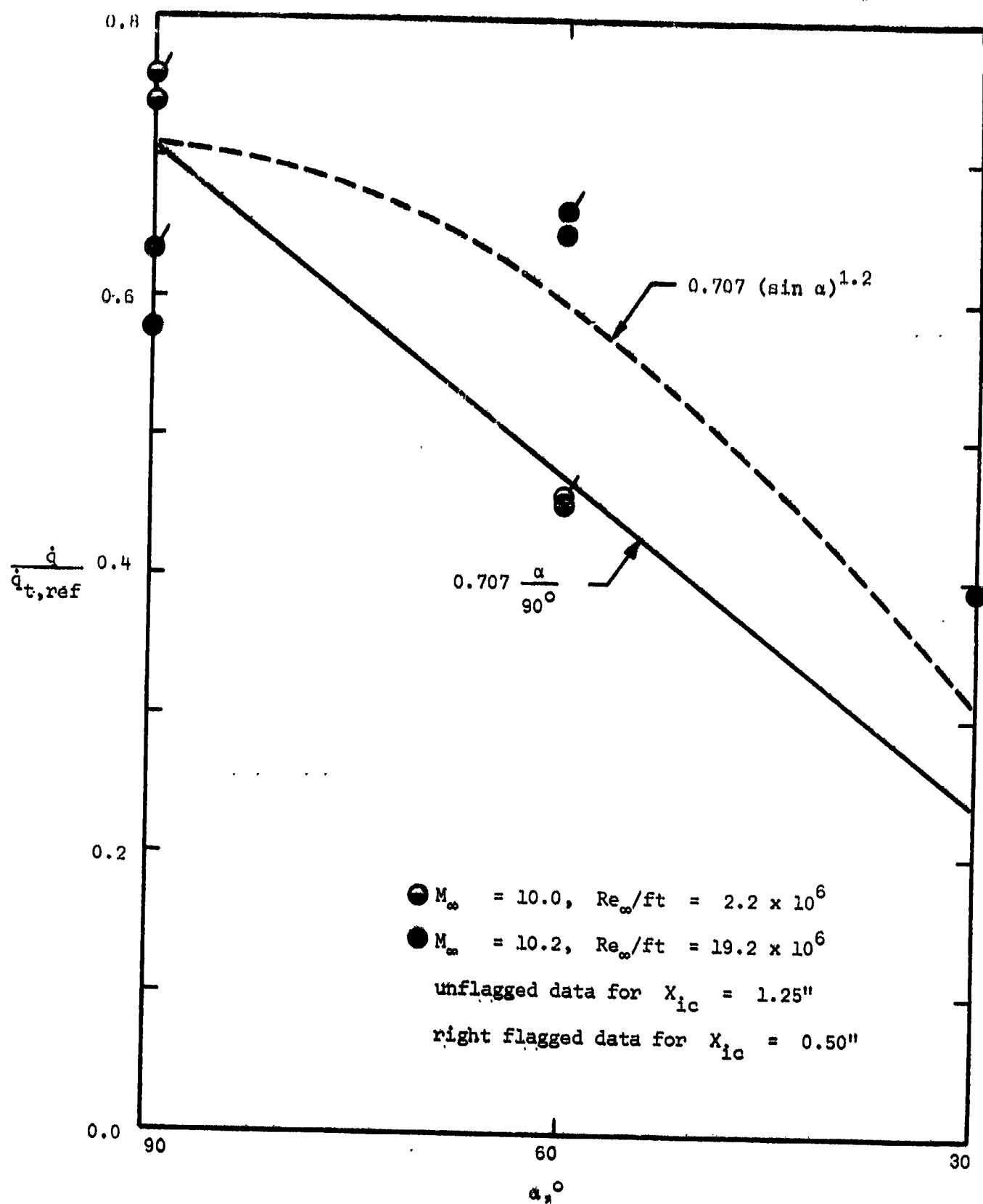
symmetry for infinite cylinders at  $\alpha = 60^\circ$



(b) Configuration C4 (rounded forebody)

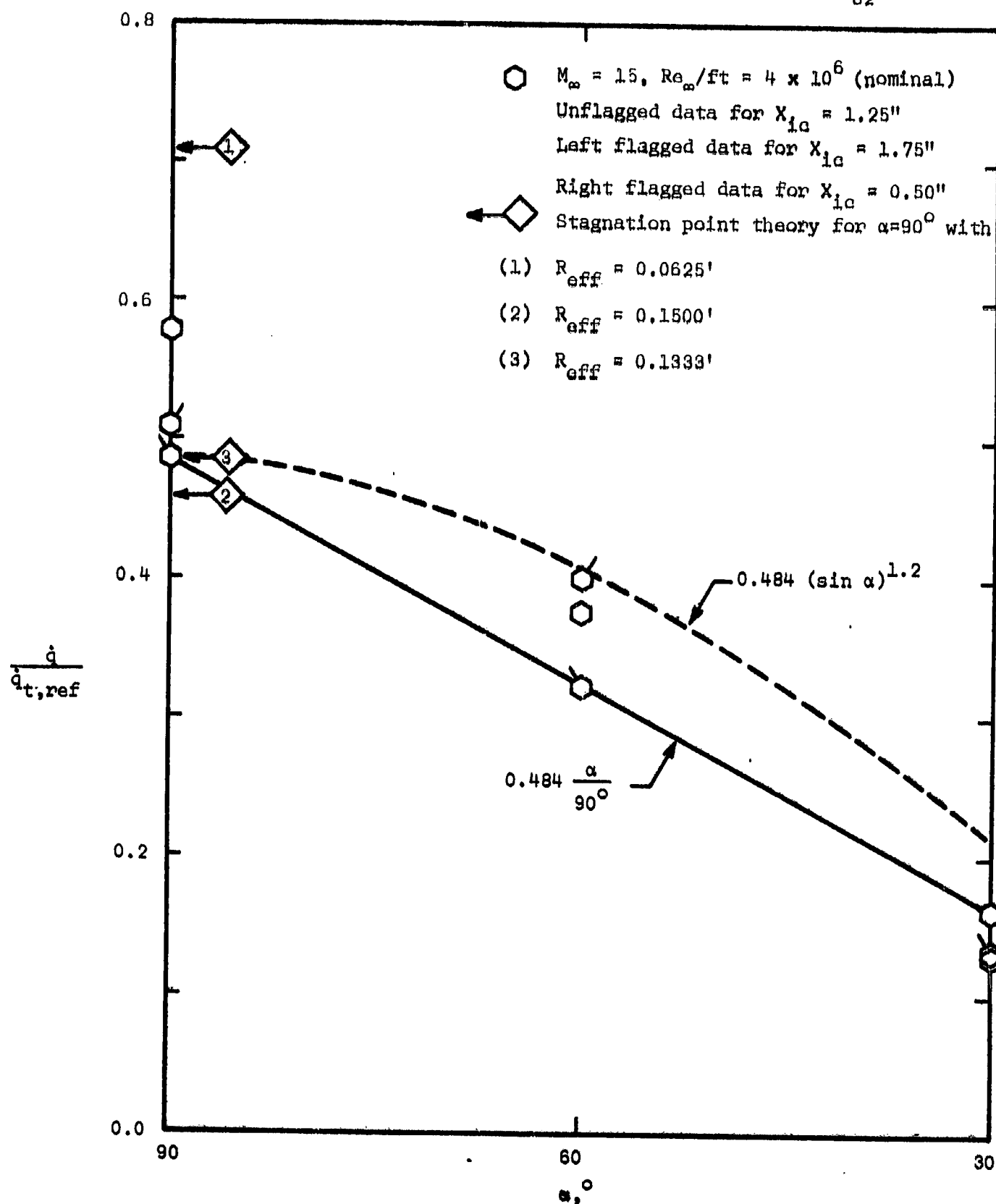
Figure 12. - Concluded.





(a) C1 - configuration

Figure 13. - Heat-transfer to the windward-most element as a function of angle-of-attack.



(b) C4 - configuration

Figure 13. - Concluded

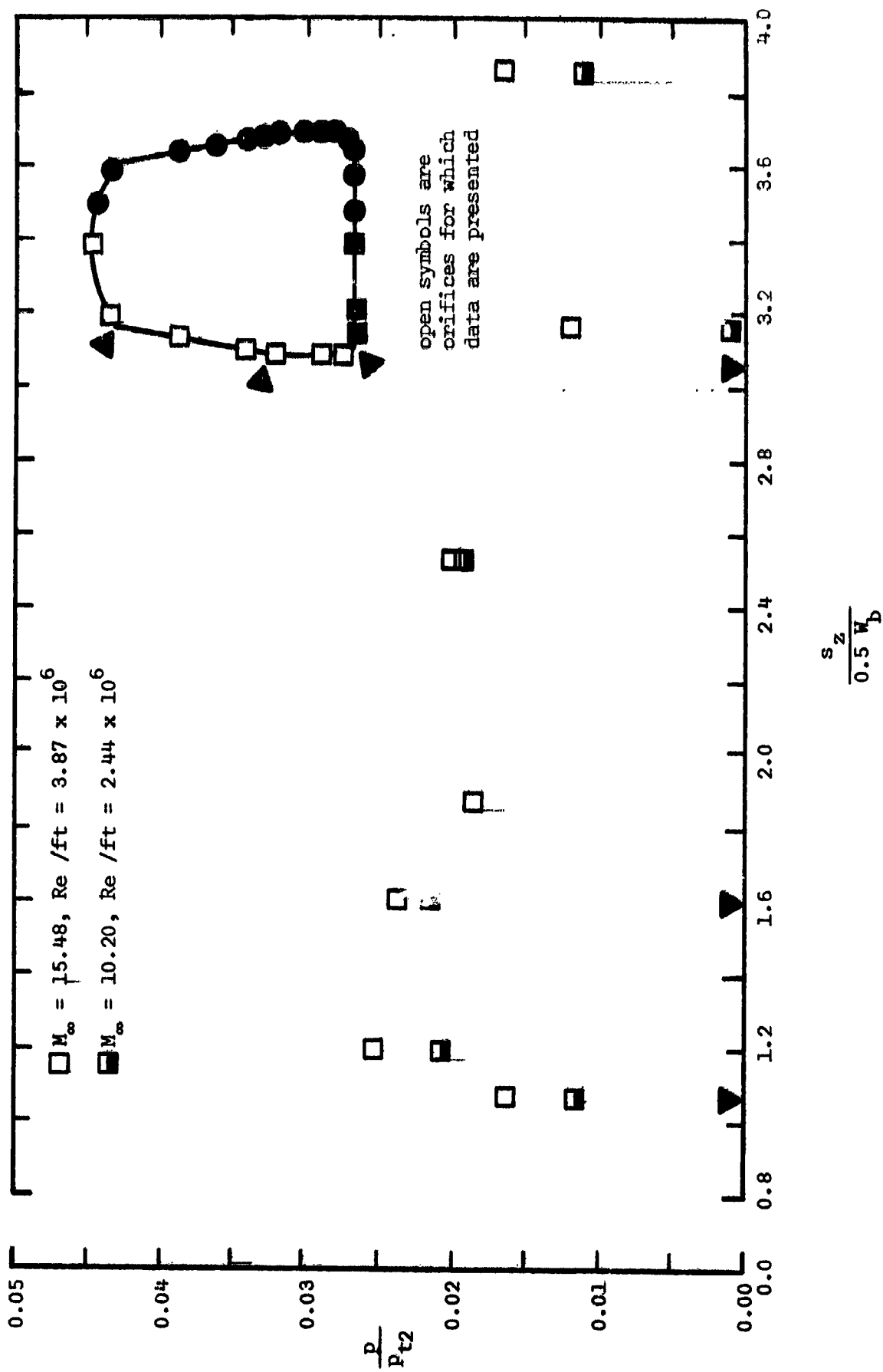


Figure 14. - Afterbody pressure distribution for the C3 cylinder.

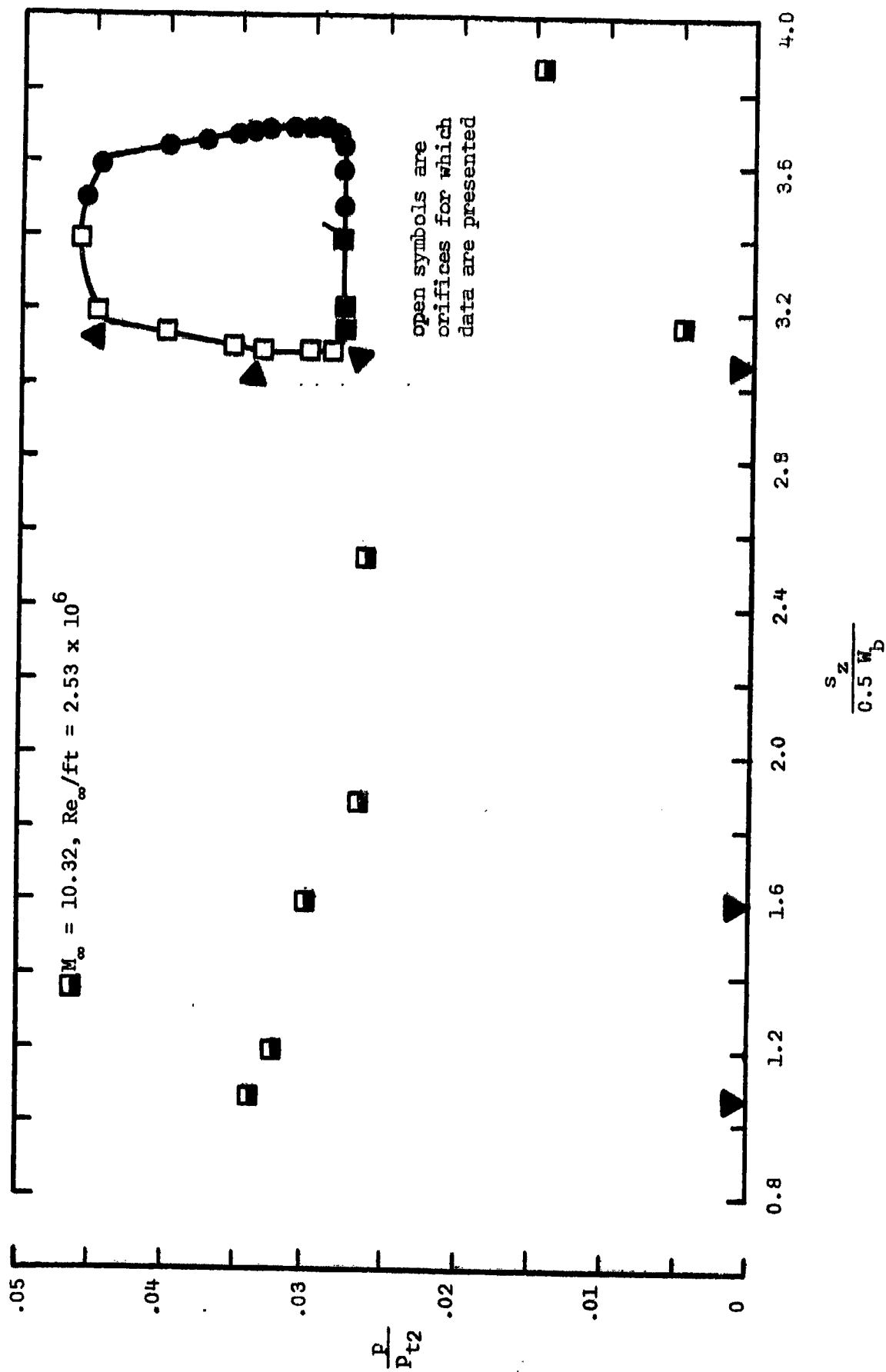
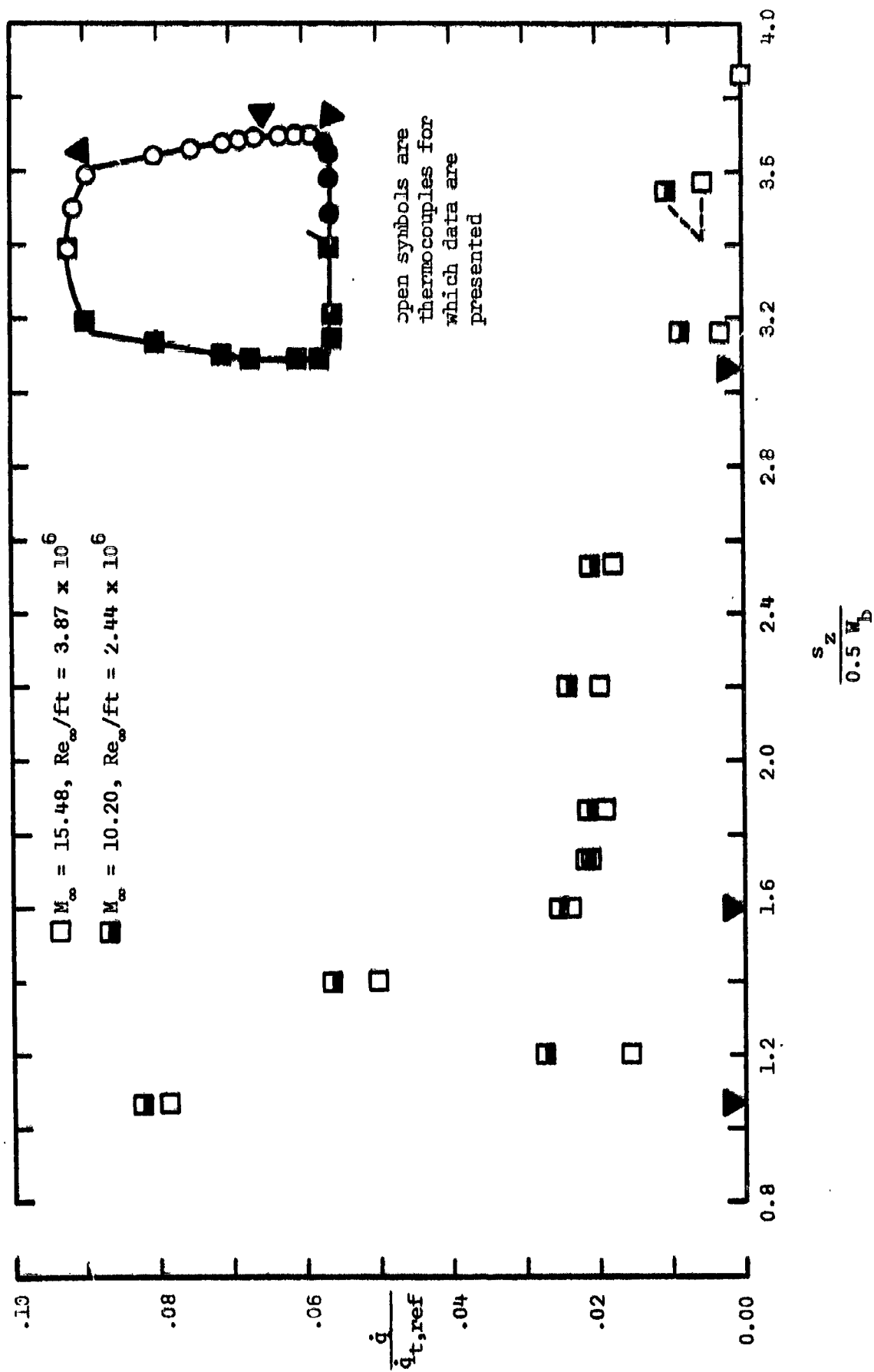


Figure 14. - Concluded



(a)  $\alpha = 60^\circ$

Figure 15. - Afterbody heat-transfer distribution for the C3 cylinder.

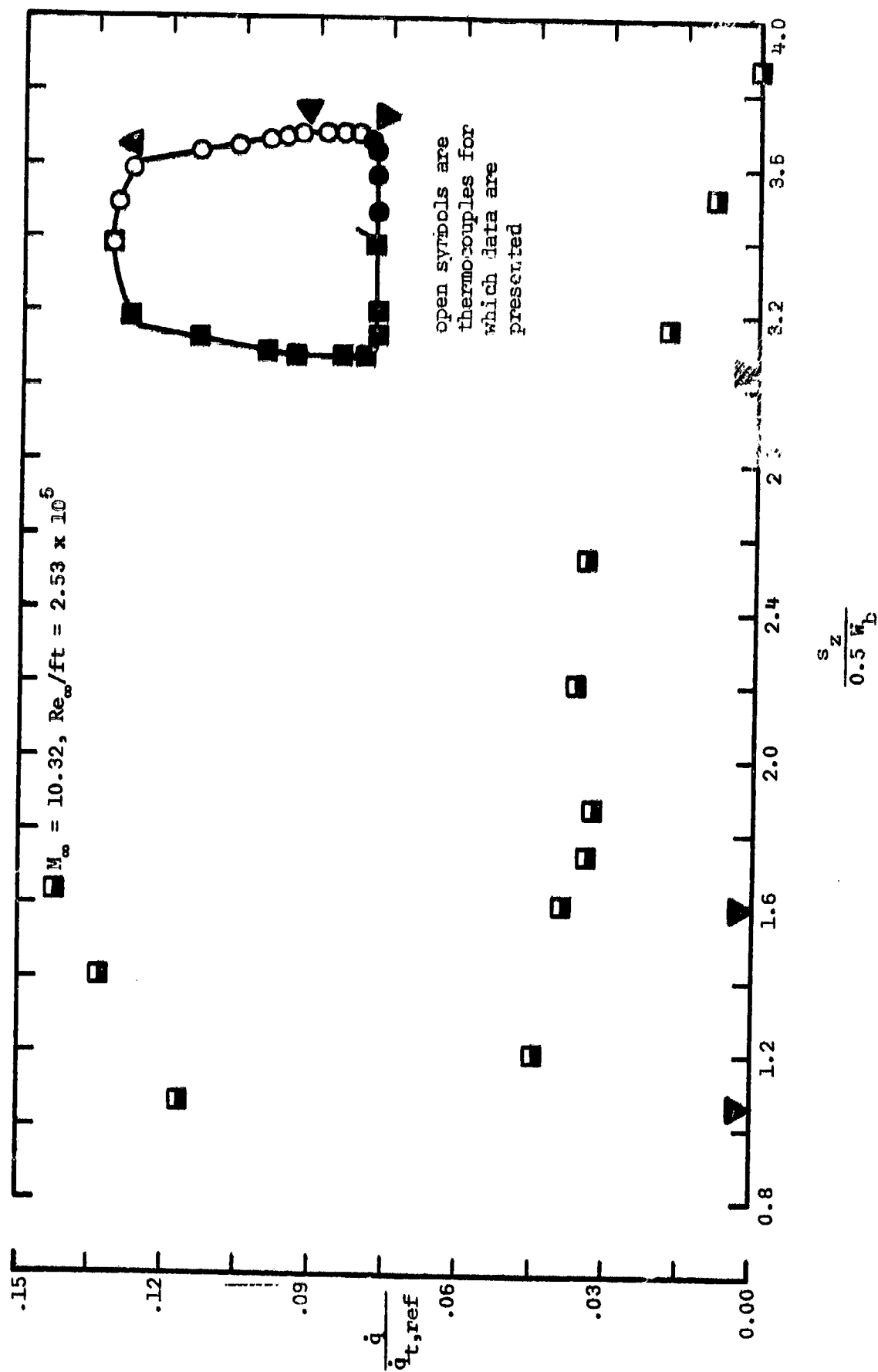
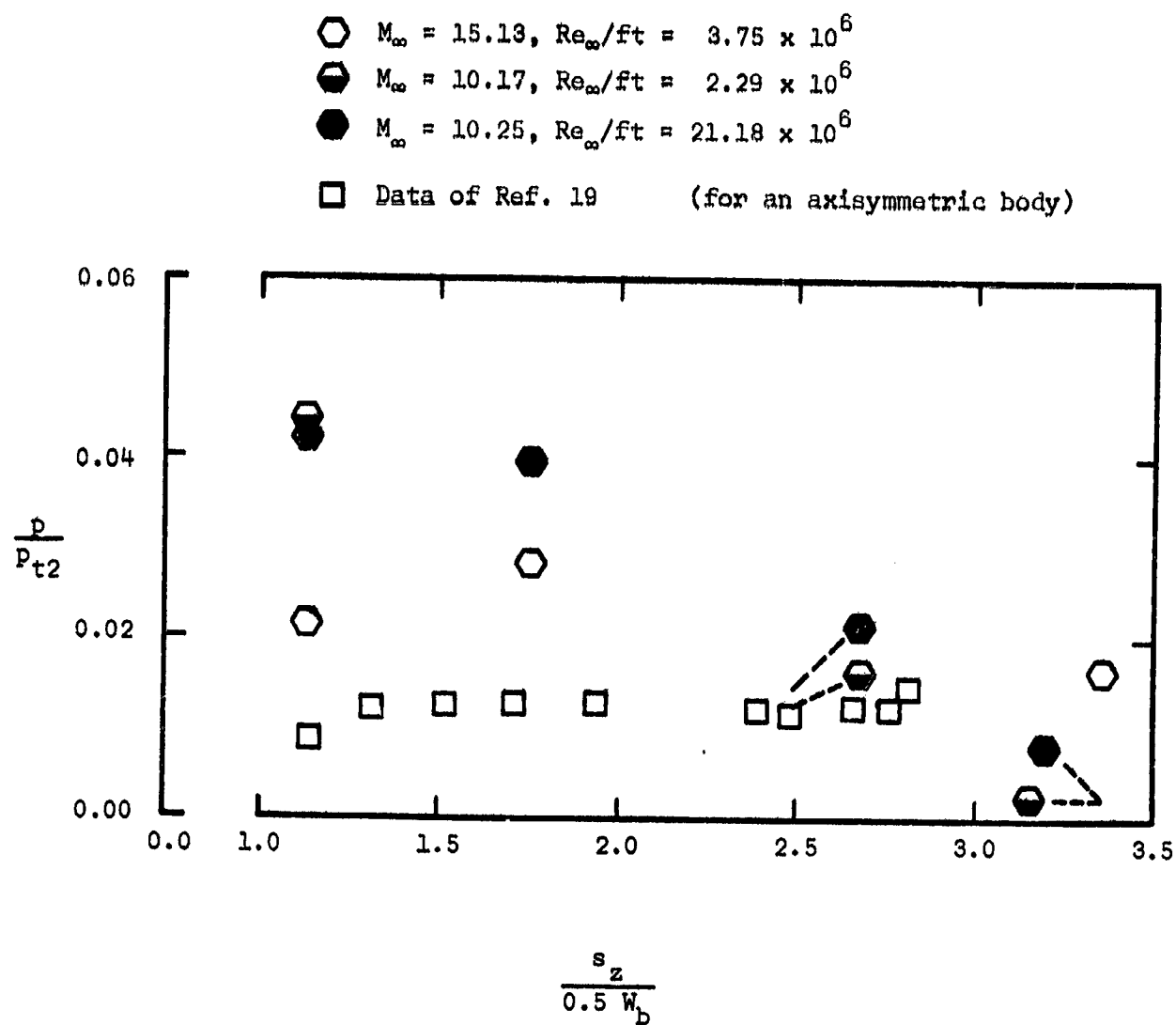
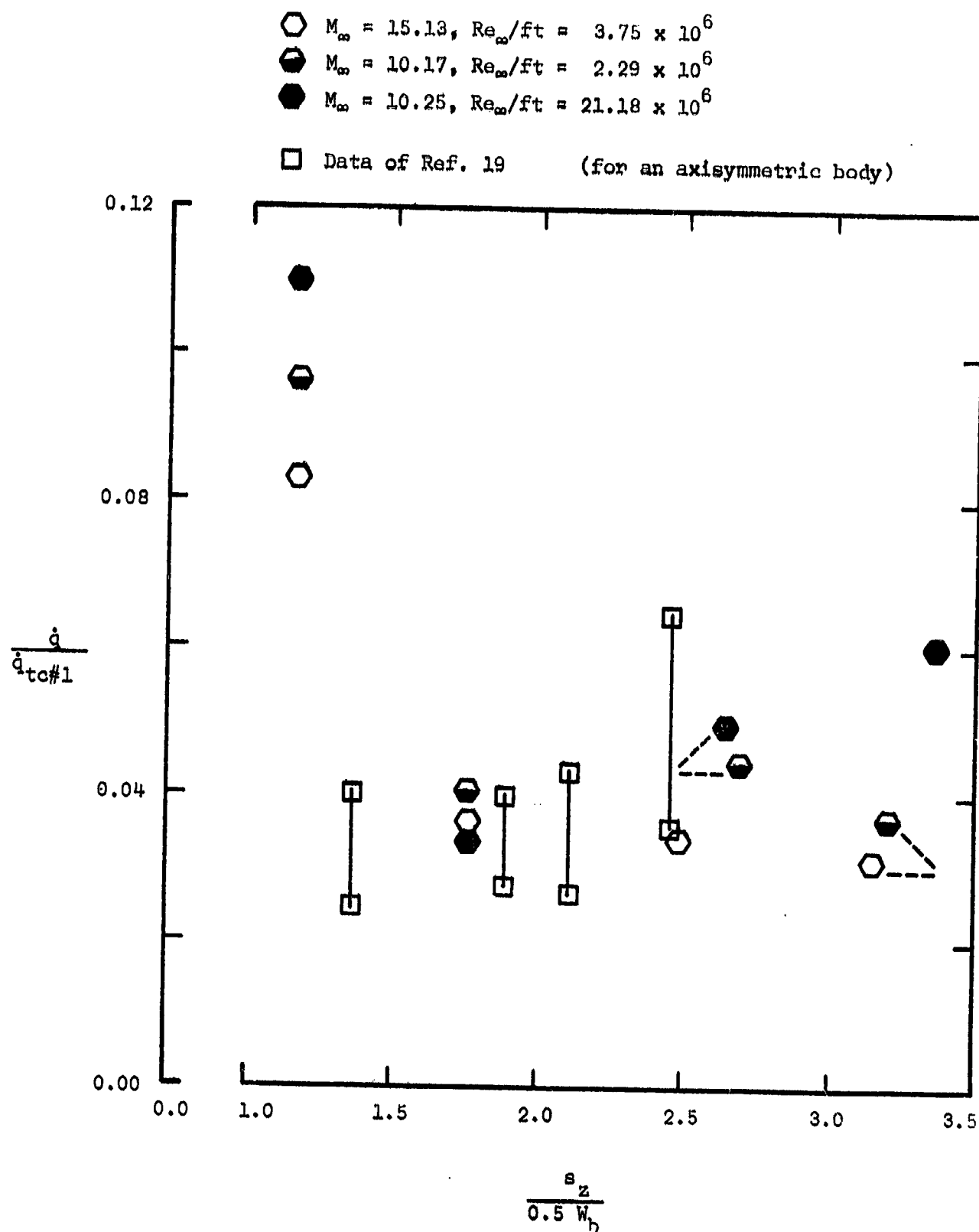


Figure 15. - Concluded.



(a) Pressures

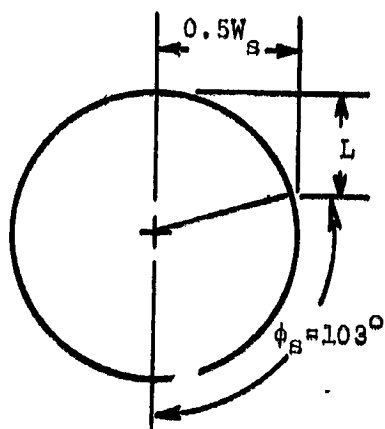
Figure 16. - A comparison of leeward data from the C4 cylinder with that for the Apollo.



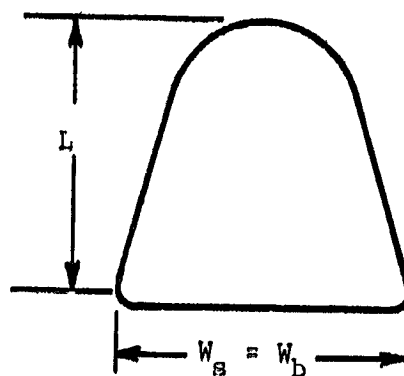
(b) Heat-transfer rates

Figure 16. - Concluded.

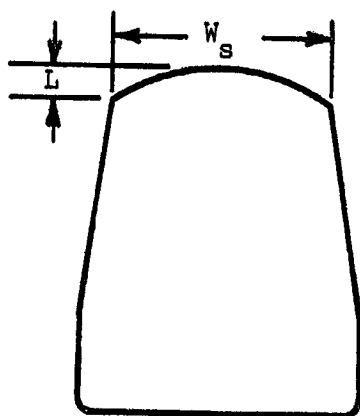




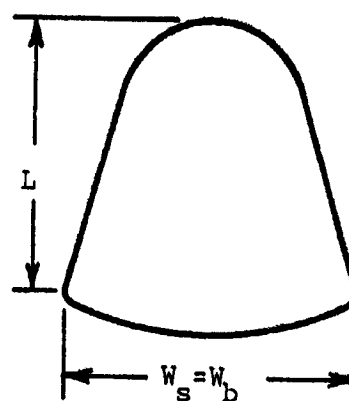
Configuration C1



Configuration C2



Configuration C3



Configuration C4

Figure 17. - Characteristic lengths ( $L$  and  $W_s$ ) of separated region for each cross section.

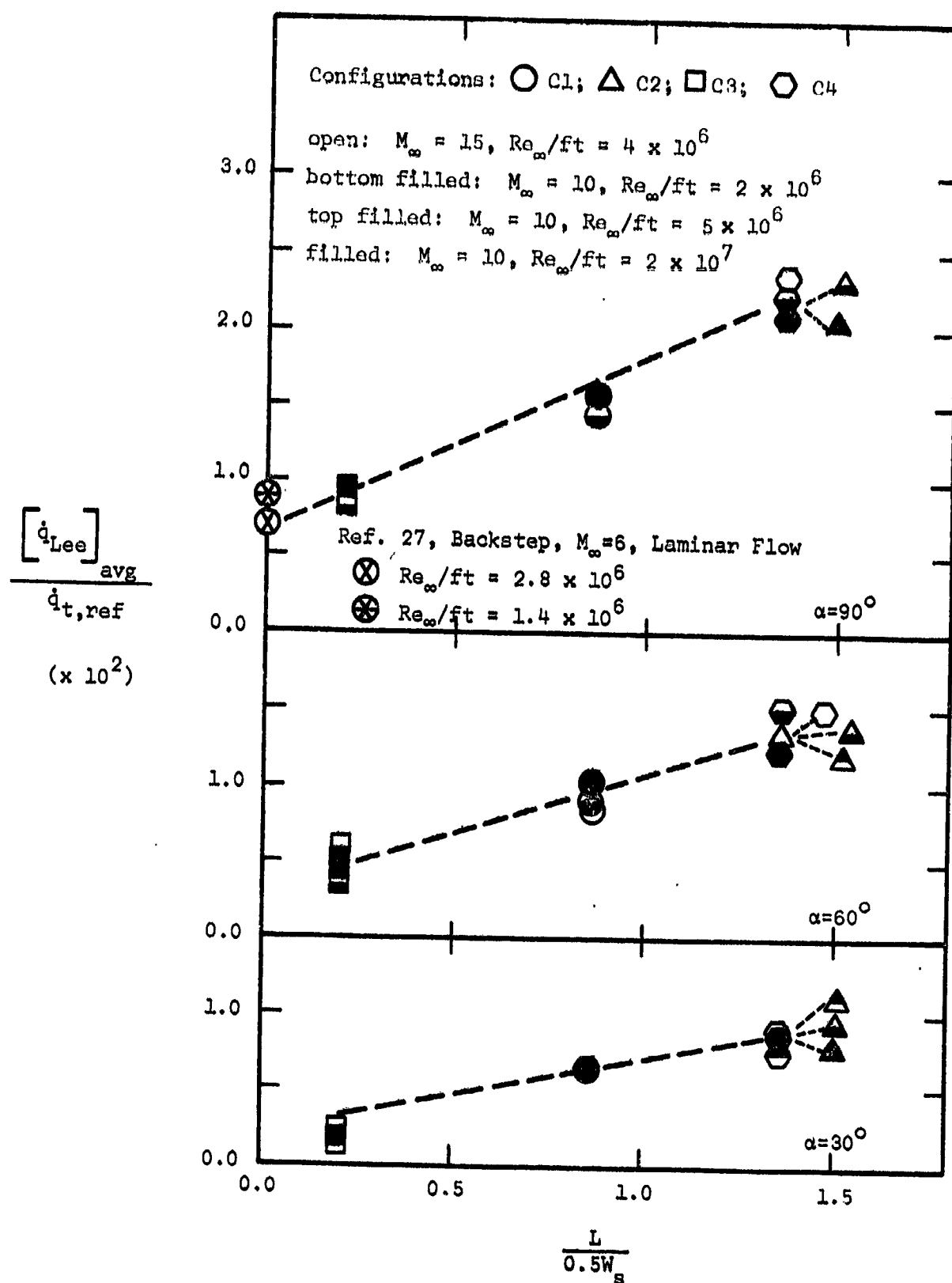


Figure 18. - Effect of leeside geometry on average leeward heat-transfer rate for various angles-of-attack.

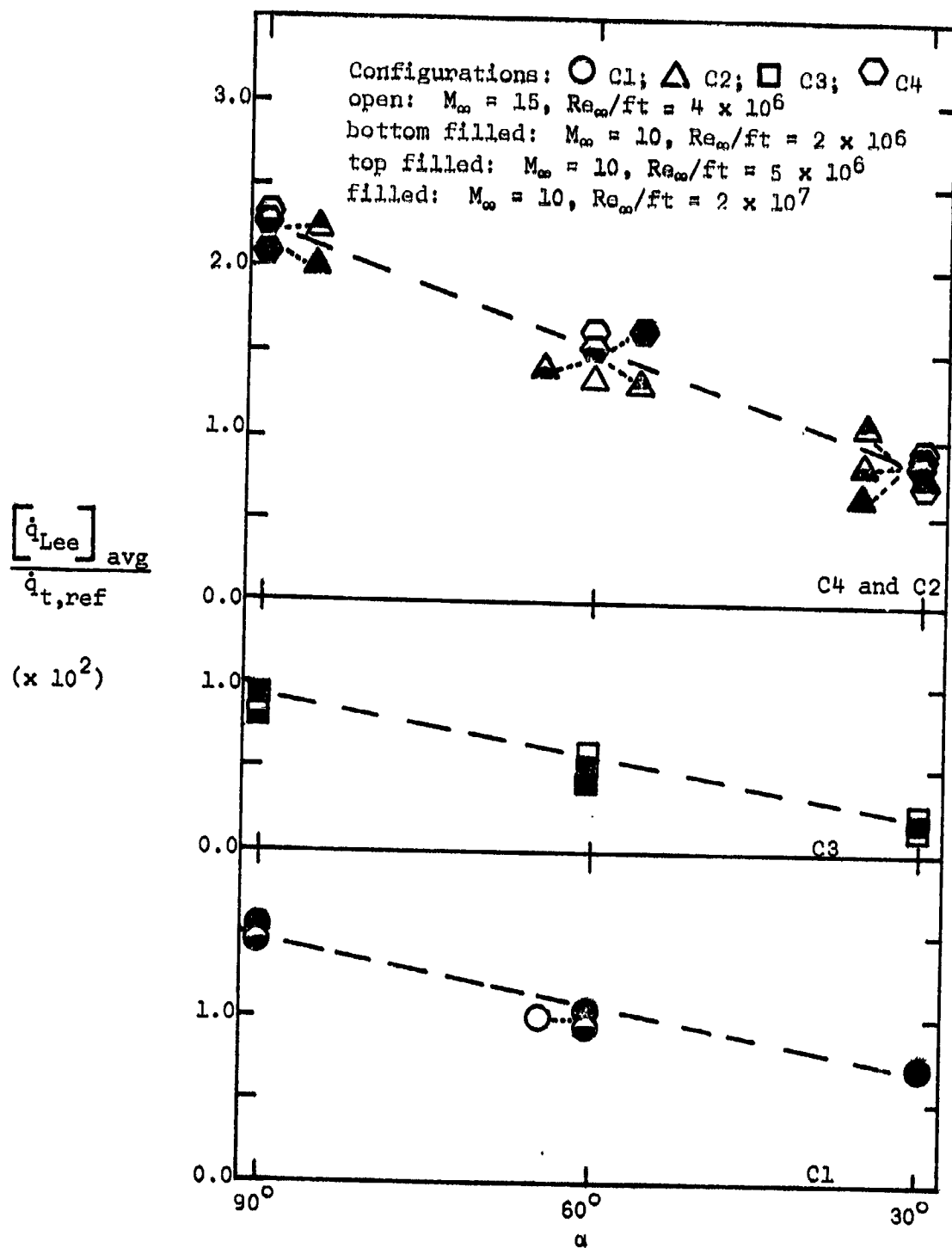


Figure 19. - Effect of angle-of-attack on average leeward heat-transfer rate for various cylinder cross sections.

REPRODUCIBILITY OF THE ORIGINAL PAGE IS POOR.

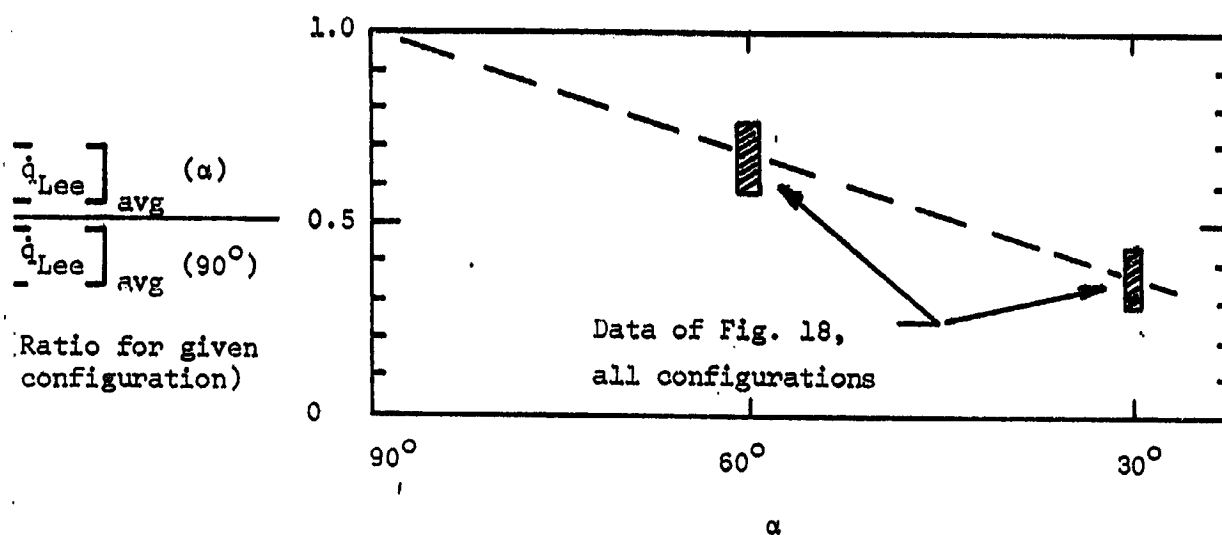


Figure 20 . - Correlation of effect of angle-of-attack on leeward heat transfer rate